Power-frequency relationship of wave dynamics in fluid-filled compliant tubes

Arian Aghilinejad, Faisal Amlani, Morteza Gharib

On the power-frequency relationship of wave dynamics in fluid-filled compliant tubes

Arian Aghilinejad*
Division of Engineering and Applied Science, California Institute of Technology, Pasadena, CA, USA

Faisal Amlani
Université Paris-Saclay, CentraleSupélec, ENS Paris-Saclay, CNRS, LMPS - Laboratoire de Mécanique Paris-Saclay, Paris, France

Morteza Gharib
Graduate Aeorospace Laboratories, California Institute of Technology, Pasadena, CA, USA

The human heart pumps in a pulsatile fashion that generates pressure and flow waves in the cardiovascular system. These waves propagate and reflect through a fractal tree network composed of fluid-filled compliant tubes. The resulting complex pressure and flow waves create a pulsatile workload (an important contributor to the pumping efficiency of the heart). Although such load has been shown to be dependent on inflow wave frequency, the fundamental relationship between power and frequency has not been directly explored. Hence the general idea of this work is to address this by modeling wave propagation in a generic pulsatile system through a fluid-structure interaction solver (based on a reduced-order Navier-Stokes formulation) applied to a fluid-filled compliant tube terminated by a controlled reflection site. We analyze the impact of reflection on such pulse waves and their associated power-frequency relationships. Our analysis considers moderate frequencies and large wavelengths as inspired by cardiovascular flows. Examining pressure-flow dynamics reveals two distinct regimes as a function of inflow frequency: a pressure-leading regime and a flow-leading regime. We observe that the latter transitions into the former at particular "optimum frequencies" that minimize the pulsatile load on the inlet and creates non-linearity in power-frequency patterns. Results suggest that the values of these frequencies strongly depend on the reflection coefficient of the tube. Our findings highlight the significance of reflection as a key determinant in design that can provide control of optimum inflow frequencies towards minimizing destructive pulsatile loads.

I. INTRODUCTION AND BACKGROUND

The propagation of waves within biological vessels induces changes in cross-sectional area and affects the time-dependent responses of fluid pressure and flow. Examples of wave sources in biological systems include the pulsatile flow that is generated by the heart in mature cardiovascular systems [1] and the impedance-based wave pumping behavior resulting from wall contractions that occur during the embryonic stage [2]. Waves generated by such sources in a physiological system travel through a fractal tree network composed of fluid-filled compliant tubes [3], encountering changes in material properties as well as vessel junctions (bifurcations) that lead to reflections [4]. The resulting complex pressure and flow profiles are determined from the interaction between these incidents (source-based) and reflected waves, leading to pulsatile loads larger than those found in non-oscillatory steady-state systems [5–8]. Abnormal levels of such pulsatile loads are well-established [9, 10] to have clinical and physiological significance in determining the health of the heart (i.e., the pulsatile inflow pump of the cardiovascular system). Indeed, the study of the underlying physics at play has garnered significant attention recently due to the valuable insights pressure and flow waves can provide into the state of biological systems [11, 12] and into the importance of ensuring optimal functionality [1, 13–16].

From a fluid dynamics perspective, analyzing the governing physics requires understanding wave propagation and reflection in fluid-filled compliant tubes. This is essential for designing systems that consist of deformable tubing and for optimizing operating conditions in order to reduce destructive pulsatile loads on the inflow generator [17]. Modeling wave dynamics and flow physics in fluid-filled elastic tubes necessitates understanding the strong interplay between the fluid and the deformable structural boundary (i.e., fluid-structure interaction, or FSI). Early studies on such configurations were conducted by Young [18], Resal [19], Moens [20], Korteweg [21] and Womersley [22]. These studies assume long wavelengths (due to their motivating applications [23]) and model only the two lowest discrete modes. These theories have since been extended to consider viscous fluid effects and infinitely many modes

* aghili@caltech.edu

of propagation [24–27]. Concurrent numerical advances and developments in more accurate experimental procedures have additionally enabled improved techniques to study such FSI problems [28–31].

A wide range of studies on wave dynamics and pumping in compliant tubes has shown that space-time variations in pressure and flow are closely linked to various wave parameters [2, 32, 33]. For instance, Jung and Peskin [34] have described the flow field and waves traveling along a tube using an immersed boundary method, highlighting a strong dependence of the net flow on the frequency of excitation. Manopoulos *et al.* [35] have investigated wave propagation due to periodic compression and decompression in compliant tubes, demonstrating resonance behavior at frequencies close to their respective natural frequencies. A similar observation has been reported by Hickerson and Gharib [33] using a one-dimensional open-loop model that corresponds well with their experimental data. Avrahami and Gharib [32] have additionally demonstrated that, at certain frequencies, the energy that is imparted on their elastic tube is converted by the fluid-structure system into kinetic energy, resulting in an efficient pumping mechanism. Other recent works have emphasized a strongly nonlinear frequency dependence of flow and pressure variations for similar FSI configurations [36–38].

Overall, it has been demonstrated that wave dynamics in compliant tubes are controlled by the fundamental frequency of the propagating waves, the material/geometrical properties of the tube (which dictate wave speeds), and wave reflection sites in the system [39, 40]. While previous studies have attempted to elucidate the complex relationship between the excitation frequency and pressure-flow variations inside fluid-filled elastic tubes, there is still an unmet need for more comprehensively investigating the effects of reflection parameters on such variations (e.g., locations and amplitudes). Indeed, wave reflection is a major component in determining the behavior of fluid-filled elastic tubes [33]. Moreover, there is evidence regarding a possible optimal wave condition that can minimize the pulsatile load on a flow generator [6, 9, 41], which suggests that studying the interplay between parameters of wave characteristics may enable more suitably-adapted design scenarios and configurations for systems of fluid-filled elastic tubes.

The goal of this work is to present a first direct study of the power-frequency relationship in a general pulsatile flow system. We approach this problem from a broad perspective by employing a most fundamental configuration: a fluid-filled compliant tube subjected to a pulsatile inflow profile with a physically-common bifurcating reflection site at the outlet (represented by two terminal tubes). The generic model proposed here enables us to examine the effect of frequency by changing the inflow profile period and enables us to examine the effect of reflection by modifying the material properties (relative to the major primary tube) of the terminal tubes at the bifurcation. We construct a reduced-order FSI model that is based on a well-established one-dimensional (2D-axisymmetric) formulation of the Navier-Stokes equations coupled with an elastic tube law. Such a model is known for its computational efficiency, having enabled previously investigation of various physical mechanisms underlying changes in pressure and flow waveforms [42, 43]. Using a high-order Fourier-based numerical solver for the governing equations of the model [44, 45] (which we further validate against reference 3D simulations), we present a comprehensive study of the interplay of major parameters related to wave dynamics and their effects on pressure and flow wave propagation. Our major focus is to investigate how the pulsatile portion of energy expenditure, which arises from the transient interplay between pressure and flow, is influenced by key parameters such as the shape of the inflow profile, frequency, and the reflection magnitude at the terminal interface. By analyzing the power-frequency relationship as a function of these parameters, this study aims to uncover insights into the optimal operating conditions for fluid-filled elastic tubes to efficiently transmit flow by determining conditions under which destructive pulsatile load is minimized. Our analysis is carried out both in the time domain and in the frequency domain (using discrete Fourier transforms). The range of parameters considered is inspired by biological vessels and covers frequency excitations of moderate amplitudes.

The manuscript is organized as follows: Section II describes the physical problem, including the governing equations, as well as the methods of analysis. Section III summarizes the numerical solver and provides corresponding validation studies. In Section IV, we present and discuss results for power-frequency trends, and our overall conclusions are presented in Section V.

II. PROBLEM DESCRIPTION

A. Physical problem

The physical problem (domain) of interest is depicted in figure 1 and consists of a straight cylindrical elastic tube (hereby known as the primary tube) of Young's modulus E, inner diameter D, thickness h, and length L filled with a fluid of density ρ and viscosity μ. Except where indicated otherwise, inner diameter D and thickness h are taken to be 0.02 m and 0.001 m, respectively. The fluid is considered to be Newtonian and incompressible with a density of 1060 Kg/m^3 and a viscosity of 0.004 Pa $\cdot$ s. Since our investigation draws inspiration from cardiovascular applications, particularly aortic biofluid dynamics, the baseline parameters are chosen to fall within average physiological ranges

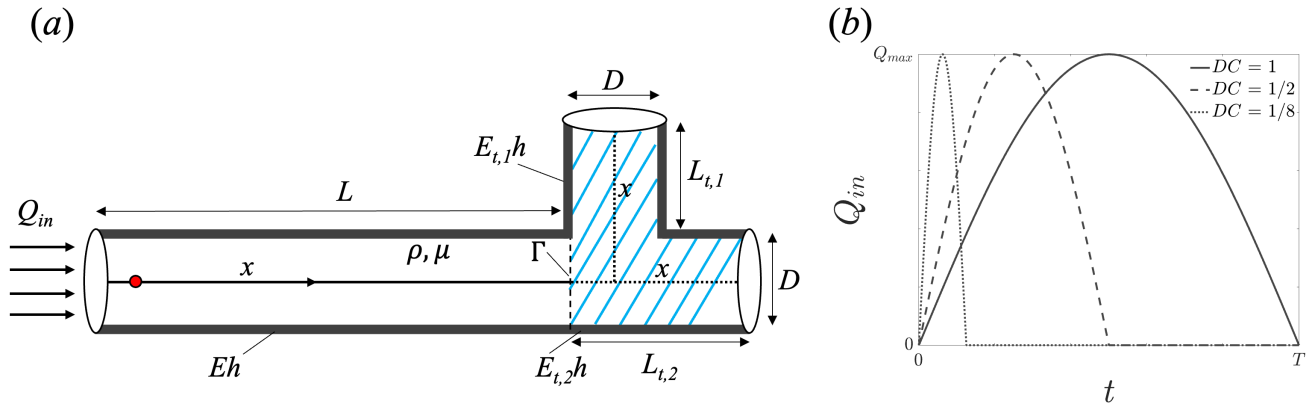

FIG. 1. (a) The physical problem of interest consisting of a straight cylindrical fluid-filled tube with the outlet connected to a reflection site (a bifurcation demarcated by a dashed line). Here, D is the diameter of the tube (and its terminals), L is the distance from the inlet to the reflection site (i.e., primary tube length), L_t is the length of the terminal tubes E (resp. E_t) is the Young's modulus of the primary (resp. terminal), h is the tube thickness, ρ is fluid density, and μ is fluid viscosity. The data collection site is indicated with red circle. (b) Examples for different duty cycles DC of the oscillatory time-dependent flow profiles applied at the inlet.

[46–48]. Inspired by the reflection sites that result from vessel (tube) junctions in physiological problems, the outlet is taken to be a bifurcation (demarcated by the dashed line) into two terminal tubes of fixed length $L_{t,1}$ and $L_{t,2}$ of 0.2 m throughout, and Young's modulus $E_{t,1}$ and $E_{t,2}$. Previous studies have shown that variations in bifurcation angle primarily influence the loss coefficient at the junction but have a minimal impact on the overall pressure and flow waveforms [49]. Since this study focuses on the flow-frequency relationship and the underlying nonlinear trends, the specific junction geometry is not explicitly considered.

As described in the next section, each segment is modelled as an axisymmetric compliant deformable tube with a single axial coordinate x (see figure 1). The primary tube bifurcates into two terminal tubes, and the dashed lines in figure 1 represent the axial coordinate for each of the three segments, which is the only spatial coordinate considered in our formulation. Since the focus of this study is on the power-frequency relationship in the primary tube, the detailed geometry of the bifurcation is not explicitly modeled. The idea of using the single axial coordinate is well-established in the context of reduced-order modeling of bifurcated tubes and is based on the cross-sectional averaged Navier-Stokes formulation. Therefore, the axisymmetric formulation is used for solving pressure-flow in each tube segment. All segments are then coupled through the characteristic equations. The wavelengths considered throughout this study are larger than the characteristic diameters of the tubes (as is the case in the biological context motivating this work). Hence a well-established [41, 50] time-dependent 1D formulation of the governing fluid-structure system is employed. Such a reduced-order model offers a good compromise between accuracy (validation studies with 3D models are provided later in this text) and computational cost. The inlet is subjected to an oscillatory time-dependent flow profile of period T given by a half-sine wave (the inflow is stationary for the rest of the interval). Such a shape is consistent with those employed in previous studies on the transient fluid dynamics of elastic tubes [1, 6, 42, 50, 51]. Figure 1 illustrates example inflow profiles for three different duty cycles (DC, the proportion of the cycle that is active and non-zero). The maximum flow $Q_{\max}$ is fixed to be 0.0001 m^3/s for the cases considered in this study (corresponding to a Reynolds number $Re = 883$).

B. Governing equations

As mentioned above, we adopt a well-established 1D nonlinear fluid-structure model for the physical problem, where pressure and flow waves propagate along a single axial coordinate [50]. The reduced-order model can be derived by conservation of mass and momentum applied to a 1D impermeable and deformable tubular control volume of cross-sectional area $A = A(x,t)$ and mean velocity averaged over the cross-section $U = U(x,t)$ (hence flow rate is given by

$Q = AU$). This yields the system of partial differential equations (PDEs) for each tube given by [1]

$$\begin{pmatrix} \dfrac{\partial A}{\partial t}\,(x,\ t) \\ \dfrac{\partial U}{\partial t}\,(x,\ t) \end{pmatrix} + \begin{pmatrix} \dfrac{\partial\,(AU)}{\partial x}\,(x,\ t) \\ U\dfrac{\partial U}{\partial x}\,(x,\ t) + \dfrac{1}{\rho}\dfrac{\partial P}{\partial x}\,(x,\ t) + \dfrac{2\,(\xi+2)\,\pi\mu U\,(x,\ t)}{\rho A\,(x,\ t)} \end{pmatrix} = 0, \tag{1}$$

where ρ is the (constant) fluid density, μ is the (constant) fluid viscosity, and ξ is a given constant of an assumed axisymmetric velocity profile (taken to be $\xi = 9$ [1]). The complete fluid-structure system is closed by an assumed elastic tube law given by [43]

$$P\,(x,t) = P_0 + \frac{\beta}{A_0}\left(\sqrt{A\,(x,t)} - \sqrt{A_0}\right), \quad \beta = \frac{4}{3}\sqrt{\pi}Eh, \tag{2}$$

where P_0 is the initial reference pressure and A_0 is the initial area (constant in x). The wall material properties are described by the value of β, which is a function of elastic modulus E (a measure of stiffness) and wall thickness h. As described in Section II A, a reflection site at the outlet of the primary tube of interest is modeled by a bifurcation (figure 1). Physically, one must enforce continuity of total pressure and conservation of mass (flow rate) at the junction point. For the main tube branching into the two terminal boundary tubes b_i, $i = 1, 2$, the corresponding mathematical conditions are given respectively by

$$P + \frac{\rho}{2}U = P_{t_i} + \frac{\rho}{2}U_{t_i}, \quad i = 1,\ 2, \tag{3}$$

$$AU = A_{t_1}U_{t_1} + A_{t_2}U_{t_2}. \tag{4}$$

These three expressions, together with enforcement of the compatibility of incoming and outgoing characteristics (derived from the corresponding Riemann invariant problem for the hyperbolic system given by equation (1) [42, 50]), provide a fully-determined system of six equations for the three unknown areas and three unknown velocities. For the numerical resolution of equations (1) to (4), this study employs a solver that is based on a high-order pseudo-spectral approach for time-dependent PDEs (Section III).

C. Analysis method

Various measures (power, reflection) are used in the results and discussion of Section IV in order to analyse pressure and flow wave profiles as a function inflow frequency. In order to quantify the proportion of the pulsatile power load over the total power generated by the waves, we study the pulsatile power ratio PPR, which is defined by

$$PPR = \frac{\frac{1}{T}\int_0^T P\,(t)\,Q\,(t)\,dt - P_{\text{mean}}Q_{\text{mean}}}{\frac{1}{T}\int_0^T P\,(t)\,Q\,(t)\,dt}. \tag{5}$$

PPR is a dimensionless parameter that compares the pulsatile contribution in the pressure-flow product to its total value, quantifying how fluctuations around the mean contribute to energy transfer. Pulsatile power over a period of T is defined as the difference between the total power (the average of the product of the inlet pressure $P(t)$ and flow $Q(t)$ over the period) and the steady power (the product of mean pressure P_{mean} and mean flow Q_{mean} over a period) carried by the pressure and flow waves. A higher PPR indicates that pulsatile dynamics dominate over steady, mean conditions, while a lower PPR suggests more uniform energy distribution. A high PPR reflects significant dynamic variability rooted in large pressure-flow fluctuations and transient effects. Its dimensionless nature enables comparisons across different systems and conditions independent of scale. Changes in the value of PPR are studied as a function of three major wave dynamics parameters, including *i*) frequency of the inflow waveform, *ii*) wave speed inside the tube, and *iii*) tube length. In addition, by changing the DC of the inlet flow profile, the impact of inflow waveform morphology on pressure and flow wave propagation is also investigated. The strength of wave reflections at the outlet can be quantified by a reflection coefficient given by

$$\Gamma = \frac{Y_p - Y_t}{Y_p + Y_t}, \tag{6}$$

where Y_p and Y_t are the respective admittances (the inverse of impedance) of the primary and terminal tubes. Admittances are calculated as $Y = A/(\rho c)$ for a wave speed c inside a tube (which is a function of Eh in the primary

and $E_t h$ in the terminal tubes, computed by the Moens-Korteweg equation [20, 21]). Note that when the primary and terminal tubes have the same geometrical and material characteristics (i.e., A and c), the reflection coefficient is zero at the bifurcation interface (an impedance-matching condition). When they do not, an impedance-mismatch occurs. In order to investigate the pressure-flow relationship for various wave conditions, we also analyze phase and power spectra. For an inflow frequency f, the phase delay $\Delta\phi = 2\pi f \Delta t$ between the pressure and flow waveforms is determined by finding the time-delay Δt using cross-correlation. For studying power spectra, the proportion of the total signal power contributed by each frequency component is determined from an application to the wave signal of the fast Fourier transform (FFT). This enables a spectral index to be defined in order to evaluate wave morphology, defined as the ratio of the power density of the second harmonic to that of the sum of the first and second harmonic [52, 53]. Ranges of the parameters employed in this work are provided in table I and are chosen based on both previous studies into fluid-filled compliant tubes as well as relevant biological studies [1, 6, 50]. For each case considered in section IV, a total of twenty periods are simulated in order to ensure that a periodic steady state has been reached.

Physical Parameter	**Unit**	**Baseline**	**Range**
frequency, f	Hz	1	[1, 8]
primary tube length, L	cm	10	[10, 30]
duty cycle, DC	-	1	[0.125, 1]
wave speed, c	m/s	1.54	[1.54, 4.62]
reflection coefficient,	-	0	[0, 0.65]
primary tube stiffness, E	KPa	50	[50, 450]

TABLE I. Physical parameters employed in this study.

III. NUMERICAL METHOD AND VALIDATION

A. Numerical method

Numerical solutions to the governing PDE system given by equations (1) and (2) are obtained by a solver based on an accelerated Fourier continuation (FC) methodology for accurate trigonometric interpolations of non-periodic functions [44, 45, 54]. High-fidelity FC-based PDE solvers have been successfully constructed and utilized for a variety of fluid dynamics problems [41]. In essence, one considers an equispaced Cartesian grid of size N on the unit interval $[0, 1]$, i.e., $x_j = (j-1)/N = (j-1)\Delta x$ for $j = 0, \ldots, N-1$ (other intervals can be considered by simple affine transformations). At a time $t = t_n$, an FC method appends a small number of discrete points in space (corresponding to an interval of size d) to the original discretized function values $A(x_j, t_n)$, $U(x_j, t_n)$ in order to form $(1+d)$-periodic trigonometric polynomials $\widetilde{A}(x), \widetilde{U}(x)$ that are of the form

$$\widetilde{A}(x) = \sum_{k=-M}^{M} a_k e^{\frac{2\pi i k x}{1+d}}, \ \widetilde{U}(x) = \sum_{k=-M}^{M} u_k e^{\frac{2\pi i k x}{1+d}} \tag{7}$$

and that match the given discrete values of $A(x_j, t_n)$, $U(x_j, t_n)$, i.e., $\widetilde{A}(x_j) = A(x_j, t_n), \widetilde{U}(x_j) = U(x_j, t_n)$, for $j = 0, \ldots, N-1$. In other words, the FC procedure adds fixed numbers of additional values to the original discretized functions in order to form periodic extensions in $[1, 1+d]$ that transition smoothly from $A(1, t_n)$ back to $A(0, t_n)$ and $U(1, t_n)$ to $U(0, t_n)$. One can interpret the resulting continued functions $\widetilde{A}, \widetilde{U}$ as sets of discrete values of smooth periodic functions that can be approximated to high-order on marginally larger intervals by trigonometric polynomials. Once such values have been determined, the corresponding Fourier coefficients a_k, u_k in equation (7) can be computed rapidly by use of FFTs. For solving equations (1) and (2), corresponding spatial derivatives for A and U at each discrete point x_j can then be calculated by exact termwise differentiation of each series in equation (7) by

$$\frac{\partial A}{\partial x}(x_i, t_n) = \frac{\partial \widetilde{A}}{\partial x}(x_i) = \sum_{k=-M}^{M} \left(\frac{2\pi i k x_i}{1+d}\right) a_k e^{\frac{2\pi i k x_i}{1+d}}, \tag{8}$$

$$\frac{\partial U}{\partial x}(x_i, t_n) = \frac{\partial \widetilde{U}}{\partial x}(x_i) = \sum_{k=-M}^{M} \left(\frac{2\pi i k x_i}{1+d}\right) u_k e^{\frac{2\pi i k x_i}{1+d}}. \tag{9}$$

The solver is completed with an appropriate time marching method, here facilitated by a fourth-order explicit Adams-Bashforth scheme (similarly to other FC-based solvers [44, 45, 54]) in order to integrate the corresponding time-domain ordinary differential equations from given initial conditions $A(x_j, t_0) = A_0(x_j)$, $U(x_j, t_0) = U_0(x_j)$ up to a given final time. The full solver ultimately provides high-order resolution of propagating waves with minimal numerical dispersion errors while incurring only mild, linear Courant-Friedrichs-Lewy constraints on timesteps [44, 45]. Further details on the FC procedure and the solver convergence can be found in Appendix A.

B. Validation study

This section compares pressure waveform profiles simulated by the 1D reduced-order model with those simulated by a standard 3D FSI solver. The reference 3D computational model employs an Arbitrary Lagrangian-Eulerian (ALE) method applied to an axisymmetric geometry consisting of a fluid domain coupled to the solid domain at the inner edge of the tube wall [55, 56]. The detailed implementation steps of the 3D ALE modeling framework can be found elsewhere [32, 57]. Sample snapshots of the spatial distribution of flow velocity generated by the reference 3D FSI model at various times during one cycle is presented in Appendix B. Figure 2 presents normalized pressure profiles generated from 3D axisymmetric ALE simulations and the 1D reduced-order simulations for four different duty cycles (1/4, 1/2, 3/4, and 1) at an inflow frequency $f = 1$Hz that is applied to a simple straight tube of length 0.2 m, diameter 0.02m, and wall thickness of 0.001m. Results suggest that the main fiducial features of the pressure profile (including waveform morphology) are well-captured using the 1D model when compared with 3D simulations. In addition to validating our reduced-order solver with a simple straight tube model, the Appendix B also presents a case with reflection at the tube outlet using the 3D FSI solver [48]. These results further demonstrate the agreement of pressure profiles for more complex test cases.

Figure 3 additionally presents the computed PPR for the 3D and 1D models at different inflow frequencies. Both models indicate a nonlinear trend in the power-frequency relation that peaks at the same frequency, further validating the use of the reduced-order solver employed in this work. The differences in the pressure profile (figure 2) and pulsatile power (figure 3) predictions arise primarily from the simplified treatment of nonlinear convective acceleration in the 1D solver [58]. At low frequencies, neglecting three-dimensional effects leads to an overestimation in power as it does not account for subtle 3D losses, while near resonance, the inability to fully capture frequency-dependent nonlinear dynamics results in underestimation compared to the 3D model. In both the 1D and 3D simulations, the system is modeled as a fluid-filled elastic tube. Using the Moens–Korteweg equation with our chosen parameters ($D = 0.02$ m, $h = 0.001$ m, $\rho = 1060$ kg/m^3, and $E = 400$ KPa), we calculate a wave speed of approximately 4.3 m/s. This speed, along with the tube length ($L = 0.2$ m), sets the expected natural frequencies. For the fundamental mode $n = 1$, the natural frequency is

$$f_{\mathrm{n}} = n\frac{c}{2L} \approx 10.8\mathrm{Hz}, \tag{10}$$

Interestingly, our results in figure 3 show a distinct resonance-like peak around 5 Hz, which is about half of the first expected natural frequency. This suggests the emergence of a subharmonic response. In fluid-structure interactions involving a compliant tube and pulsatile flow, nonlinearities can give rise to subharmonic resonances, where energy concentrates at frequencies that are fractional multiples of the fundamental mode [59, 60]. These findings suggest that both models (1D and 3D) exhibit a matching nonlinear resonance at around 5 Hz that is not only consistent with the complex physics of the coupled fluid-tube system but also confirms that the simplified approach used here can reliably represent these nonlinear dynamic phenomena. In the following sections, all the results are obtained using the 1D solver.

IV. RESULTS AND DISCUSSION

A. Impedance-matching at the reflection interface

Figure 4 presents simulated pressure and flow waveforms (close to the primary tube inlet and after reaching an oscillatory steady-state) that are generated by various inflow frequencies f. The reported pressures are non-dimensionalised by scaling with $\rho U_{\max}^2$ (where $U_{\max}$ represents the maximum inflow jet velocity), and flows are non-dimensionalised by scaling with $Q_{\max}$. In order to isolate the effect of frequency, baseline values have been used for all other parameters, i.e., a fixed duty cycle, tube length, and wave speed corresponding to the appropriate column in table I. Additionally, in order to ensure impedance matching at the tube interface, the same material properties have been used for both the primary and terminal tubes ($\Gamma = 0$). Results indicate that even with fixed-shape inflow waveforms and fixed

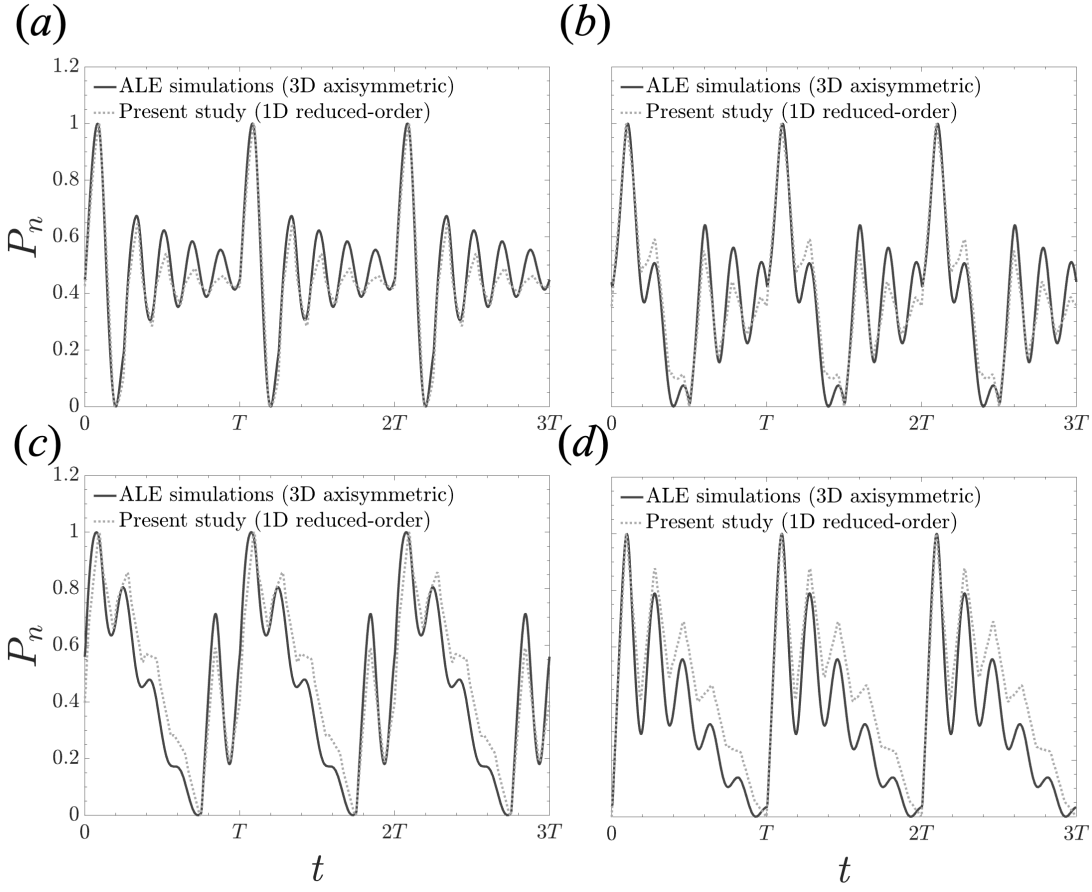

FIG. 2. Normalized pressure waveforms P_n at the inlet for a simple straight fluid-filled compliant tube simulated by the solver employed in this paper (dotted line) and by a 3D FSI solver (solid line) at duty cycles of (a) 1/4, (b) 1/2, (c) 3/4, and (d) 1. Results correspond to a flow source at a frequency of $f = 1$ Hz (see figure 1).

tube characteristics, there is a strong frequency-dependence that leads to appreciable changes in both amplitude and morphology (shape) of the corresponding pressure waveforms. The power spectrum of these four pressure profile is presented in Appendix C for reference. Results indicate that even with fixed-shape inflow waveforms and fixed tube characteristics, there is a strong frequency-dependence that leads to appreciable changes in both amplitude and morphology (shape) of the corresponding pressure waveforms. However, as indicated by the dotted line, the average value for the normalized pressure waveform over the cycle remains almost constant (= 0.899). Although the instantaneous values of normalized pressure fluctuate between 85 and 95 throughout the cycle, the mean value over one full cycle remains nearly constant, as indicated by the dotted line. Since the inflow profile is identical across all cases presented in this figure, the mean value for the flow remains unchanged. The negative values observed at f=4 Hz arise due to phase shifts inherent to pulsatile waveforms at higher frequencies and do not affect the cycle-averaged mean flow. Therefore, changes in the waveform morphology result in alterations to the pulsatile portion of the power.

Figure 5 presents simulated PPR as a function of frequency f for different primary tube lengths (i.e., different locations of the reflection site) generated by the same-shaped inflow waveform of duty cycle $DC = 1$. Although a strong frequency-dependence of the power can be observed, mean values for pressure and flow remain nearly constant (cf. figure 4). That is, the steady contribution to power is the same across frequencies for fixed duty cycle, tube length, and wave speed. Thus, changes in PPR can be attributed to variations in the pulsatile contribution (i.e., the waveform morphology), where figure 5 further suggests that the frequency-dependence of power is non-linear and strongly influenced by the tube length. Since wave speed remains constant across these cases, changes in the tube length will only affect wave travel time (L/c), altering the interaction between forward-running pressure and flow waves (generated at the primary tube inlet) and backward-running waves (reflected from the terminal tube outlets). This impacts the shape of the pressure waveform, subsequently influencing pulsatile power. Additionally, specific frequencies can be clearly identified to exist in figure 5 at which the PPR on the inflow generator is minimal (hereafter referred

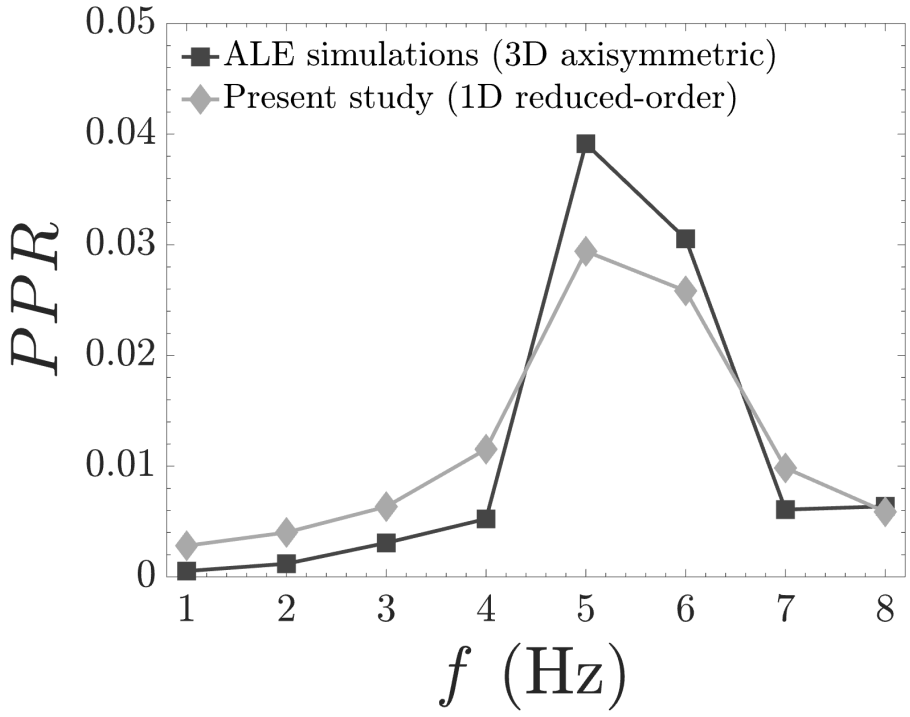

FIG. 3. The pulsatile power ratio (PPR) at different inflow frequencies f for a straight tube using both the 1D reduced-order model of this study (dashed line) and a 3D axisymmetric ALE model (solid line).

to as optimum frequencies, or f_0). Such minima are particularly evident for the cases corresponding to primary tube lengths of $L = 2l_{\text{base}}$ and $L = 3l_{\text{base}}$, and non-existent at the $L = l_{\text{base}}$ case for the studied mid-range frequencies-of-interest (see table I). When the tube length increases (e.g., from l_{base} to $3l_{\text{base}}$) while maintaining constant wave speed and other tube characteristics, the fundamental natural frequency decreases, leading to a reduction in the spacing between harmonics (see equation 10). This behavior is analogous to that observed in vibrating strings, where increasing the length results in closer harmonic spacing. In our system, this change in harmonic structure alters the interaction between incident and reflected waves within the tube. The modified interference patterns shift the frequencies at which constructive and destructive interferences occur, thereby affecting the energy exchange and PPR. Specifically, the positions of minima and maxima in the PPR-frequency relationship are displaced due to the length-induced changes in natural frequencies and harmonic spacing. Additionally, the nonlinear nature of the fluid-structure interactions within the compliant tube contributes to the complexity of the PPR-frequency trend. Nonlinear effects can lead to phenomena such as subharmonic resonances (as shown in figure 3), further influencing the observed PPR variations. Similar non-linear behavior has been observed in previous computational and experimental studies on the power-frequency pattern of pulsatile flow in the aorta [6]. For example, Pahlevan and Gharib [61], using a hydraulic circuit model of the human vascular system, demonstrated the existence of an optimum heart rate (i.e., the fundamental frequency of cardiovascular waves) at which pulsatile workload is minimized. These findings are consistent with the results of the present study, which also identifies, but more generally, a frequency-dependent minimum in pulsatile power within a compliant fluid-filled tube subjected to pulsatile inflow.

The top row of figure 6 further investigates these optimum frequencies by examining the phase delay between pressure and flow. As before, all simulations are sourced by the same-shaped inflow waveform (i.e., the same duty cycle of $DC = 1$). Results indicate the presence of two distinct regimes of inflow frequencies characterized by the phase delay (negative or positive). A negative phase delay signifies that the pressure peak wave leads the flow wave in time (pressure-leading regime), whereas a positive phase delay indicates that the flow peak wave leads the pressure wave in time (flow-leading regime); illustrative examples of these definitions can be found in the Appendix (figure 18). In this work, the phase relationship is determined using the overall time shift identified through cross-correlation, rather than focusing on the foot of the waveforms. One of the primary objectives is to investigate the impact of wave reflections on the global phase relationship. The cross-correlation method is chosen since it effectively captures timing shifts across the entire waveform, providing a more comprehensive analysis compared to just isolating the foot. This approach aligns with our goal of understanding how wave reflections influence the global dynamics of the

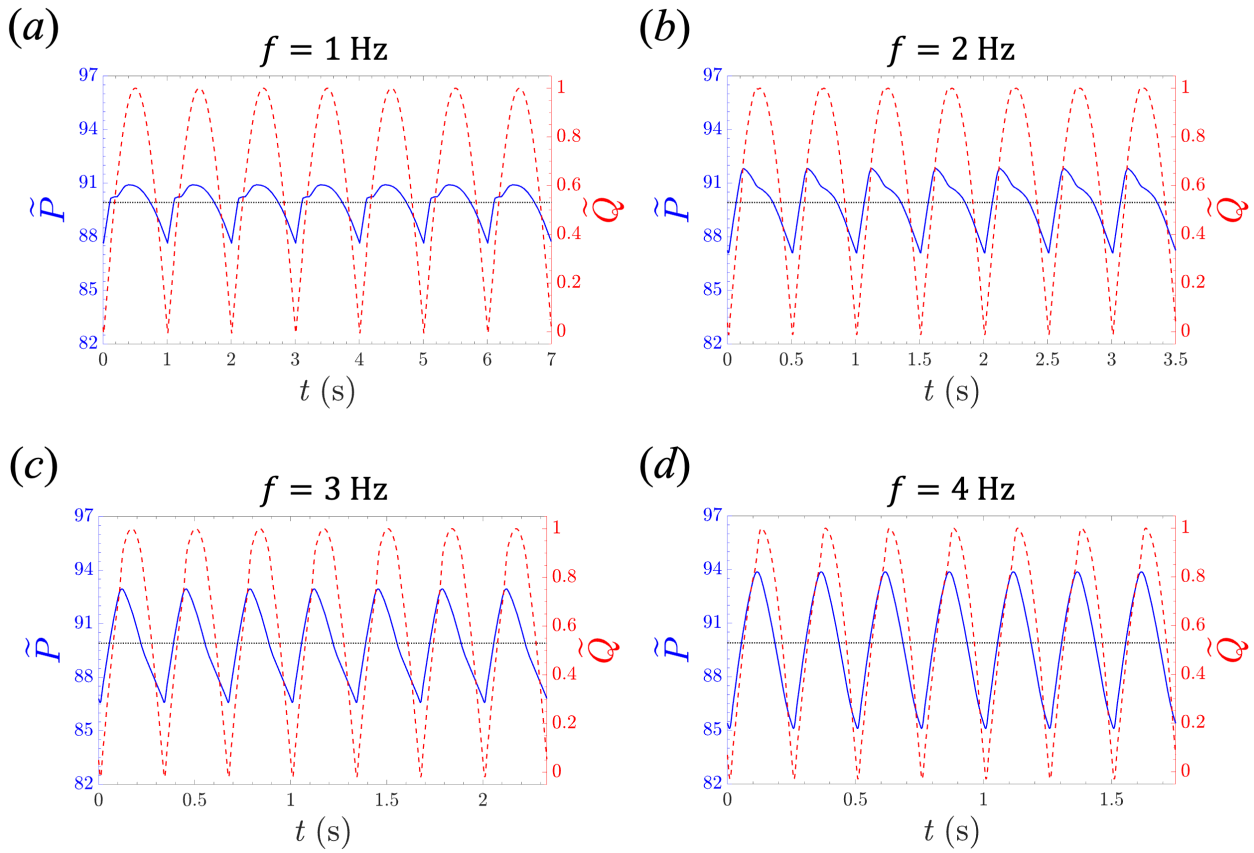

FIG. 4. Pressure (solid lines) and flow (dotted lines) waveforms at the data collection site (see figure 1) after reaching an oscillatory steady-state for inflow frequencies of (a) 1 Hz, (b) 2 Hz, (c) 3 Hz, and (d) 4 Hz. Dotted line indicates the mean value for the pressure waveform over the cycle. Pressure is non-dimensionalised by $\rho U_{\max}^2$ and flow is non-dimensionalised by $Q_{\max}$.

waveform. As inflow frequency increases at the baseline tube length (figure 6), wave morphology transitions from a pressure-leading regime to a flow-leading regime, with no observable optimum frequency in the range-of-interest (consistent with figure 5). However, for the cases of tube lengths $L = 2l_{\text{base}}$ and $L = 3l_{\text{base}}$ (figure 6), the phase delay oscillates between the two regimes as a function of frequency. The frequencies at which the phase transitions from flow-leading to pressure-leading correspond exactly to the minima of the PPR curves of figure 5, i.e., the points of optimum frequency. Conversely, the frequencies at which phase transitions from pressure-leading to flow-leading correspond to the maxima of the PPR curves. Hence the frequencies at which either transition occurs correspond to the extrema in PPR. These results highlight the importance of examining the pulsatile portion of energy expenditure as a sensitive metric influenced by various wave parameters. Specifically, the dimensionless nature of the PPR enables consistent comparisons across systems and conditions of varying scales.

In order to investigate the effects of frequency on waveform morphology, the bottom row of figure 6 additionally presents the spectral index of the pressure and flow profiles corresponding to the three different lengths of the top row (i.e., different reflection site locations). Across all cases, the spectral index remains consistently below 0.5, indicative of the predominance of the first harmonic. However, there are discernible fluctuations in the significance of the second harmonic when changing inflow frequencies. These fluctuations imply a non-linear association between pressure-flow profile shape and inflow frequency. Furthermore, we observe that alterations in waveform shape are more pronounced in the pressure profile. The optimum frequency occurs when the spectral index values for pressure and flow profiles converge, with the spectral index of the pressure reaching its local minimum. The alignment of waveform shapes at zero phase delay reflects the transition from a flow-leading to a pressure-leading regime. The local minimum in the spectral index of pressure suggests that the shape of the pressure profile is primarily influenced by the first harmonic (induced by the inflow wave), resulting in reduced pulsatile load on the input. This pattern elucidates the presence of the optimal frequency at the transition from the flow-leading regime to the pressure-leading regime.

For the same tube lengths (i.e., reflection sites), figures 7 and 8 presents PPR, phase delay, and spectral index

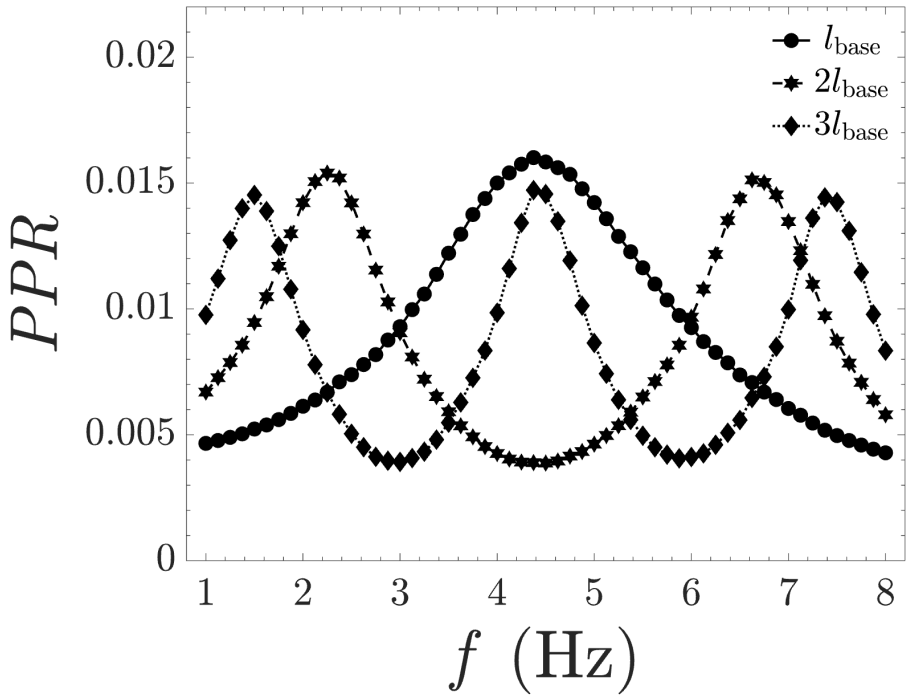

FIG. 5. The pulsatile power ratio (PPR) as a function of frequency f for three tube lengths that are multiplicative factors of the baseline length l_{base} given in table I. For all simulations, the same inflow waveform of duty cycle $DC = 1$ and the same reflection coefficient of $\Gamma = 0.0$ have been employed.

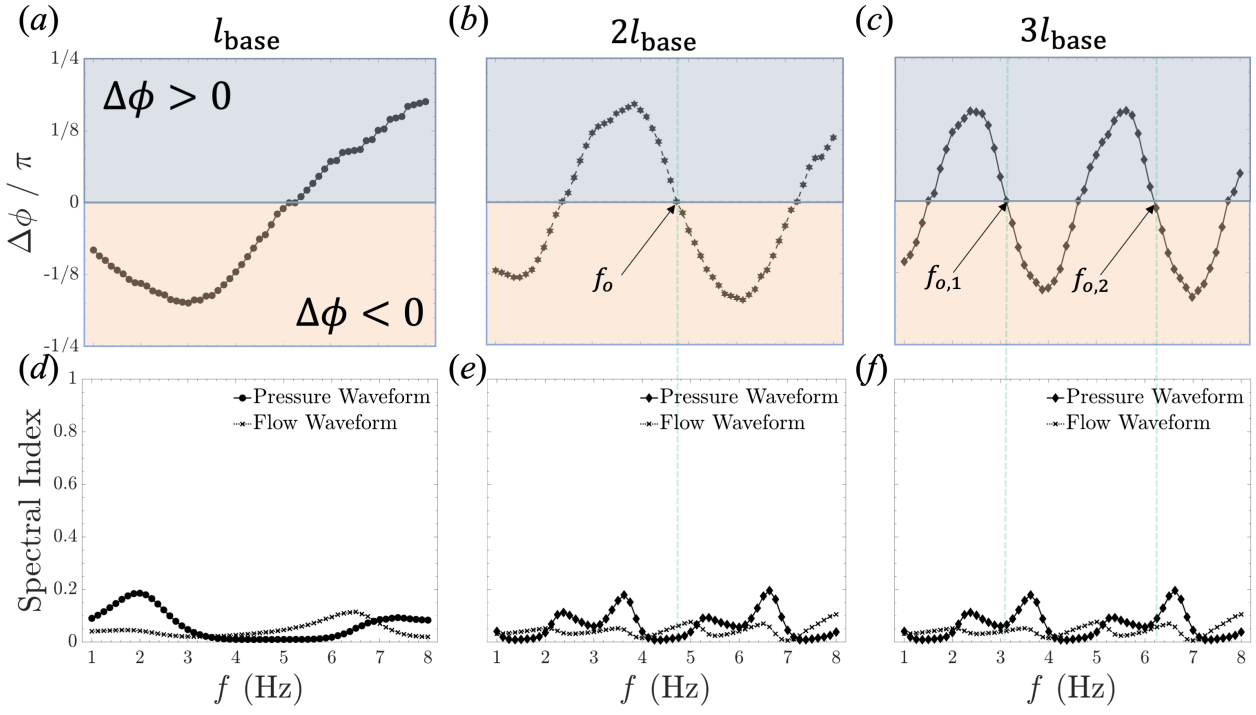

FIG. 6. The pressure-flow phase delay between (top row) and the spectral index (bottom row) as a function of inflow frequency for baseline primary tube lengths ((a) and (d)), twice the baseline ((b) and (e)), and three times the baseline ((c) and (f)). The green dashed lines demarcate the location of the optimum frequencies. For all simulations, the same inflow waveform of duty cycle $DC = 1$ and the same reflection coefficient of $\Gamma = 0.0$ have been employed.

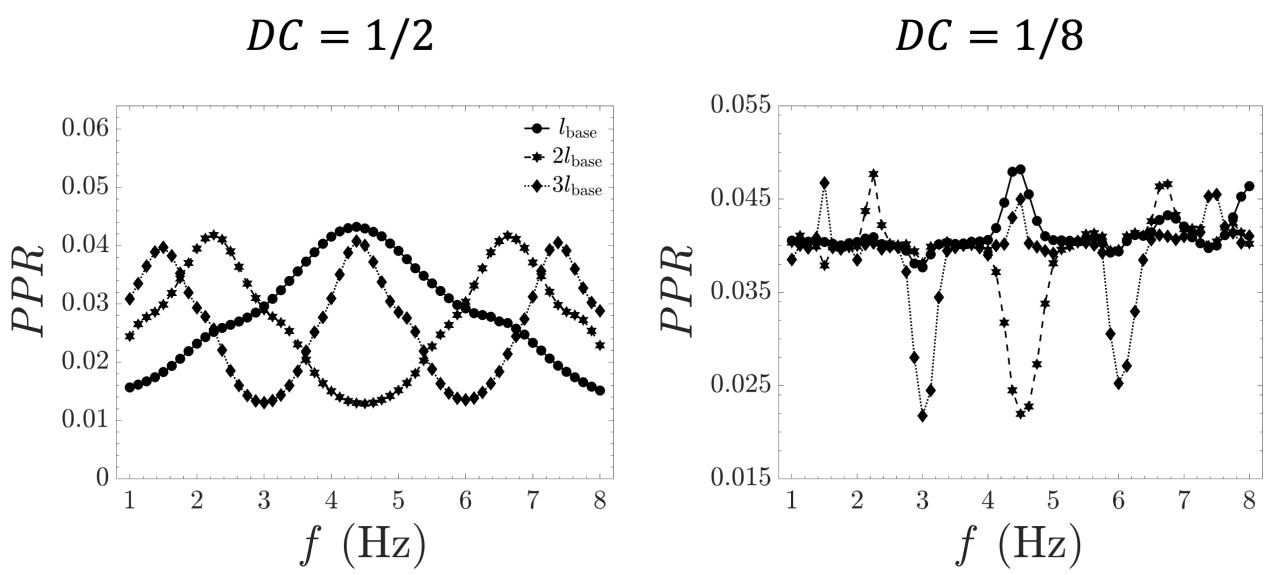

FIG. 7. The pulsatile power ratio (PPR) as a function of frequency f for three tube lengths that are multiplicative factors of the baseline length l_{base} given in table I. Simulations were performed for two inflow waveform profiles with duty cycles of values $DC = 1/2$ and $DC = 1/8$.

as a function of inflow frequency corresponding to two other duty cycles (i.e., different shapes of the inflow wave). Results suggest that changing the shape of the inflow wave profile does not strongly affect the pressure-flow phase delay, and, consequently, the optimum frequency of the system remains unaffected (cf. figures 5 and 6). However, altering the inflow profile does appear to affect the PPR amplitude, which can be attributed to the correspondingly significant changes in morphology of the pressure and flow waveforms. In particular, for smaller duty cycles, the effect of reflected waves is more pronounced, leading to inflow frequencies where the second mode largely dominates the source's fundamental harmonic. Our analysis shows that while the inflow profile affects the amplitude of the PPR, the pressure-flow phase relationship is primarily governed by wave speed and tube length—intrinsic characteristics of this nonlinear system—with minimal influence from the inflow profile shape of the system's input.

B. Impedance-mismatching at the reflection interface

Figure 9 presents PPR as a function of frequency for different primary tube lengths at a reflection coefficient of $\Gamma = 0.5$. For a fixed wave speed, such a reflection coefficient can be achieved by inducing an impedance mismatch at the primary tube outlet (bifurcation interface) by increasing the stiffness nine-fold of each terminal boundary tube while keeping the primary stiffness at baseline. A change in cross-sectional area can also achieve different reflection coefficients, but wave speed is simultaneously affected. Results suggest a distinct difference in the power-frequency trend between the data in figure 9 ($\Gamma = 0.5$) and that corresponding to figure 5 ($\Gamma = 0$, i.e., impedance-matching), where the former has an optimum frequency minimizing PPR (no such minimum clearly exists for the frequencies-of-interest in the impedance-matching case). For the same inflow source, primary tube length, and wave speed, this indicates that alterations in outlet wave conditions (which affect interactions between forward- and backward-running wave components) can induce optimized/minimized power loads on the inflow generator. Furthermore, the frequencies at which such minima are achieved can be controlled by wave reflections, as can be seen for the $2l_{\text{base}}$ and $3l_{\text{base}}$ cases in figure 9 (cf. figure 5). Appendix C further presents the calculated phase delays between pressure and flow at a reflection coefficient of $\Gamma = 0.5$. A similar observation can be made to that of the case for $\Gamma = 0$ (Section IV A): the optimum frequencies that minimize the pulsatile load on the inlet flow generator (figure 9) occur at the transition from a flow-leading frequency regime to a pressure-leading regime (positive phase difference to negative phase difference).

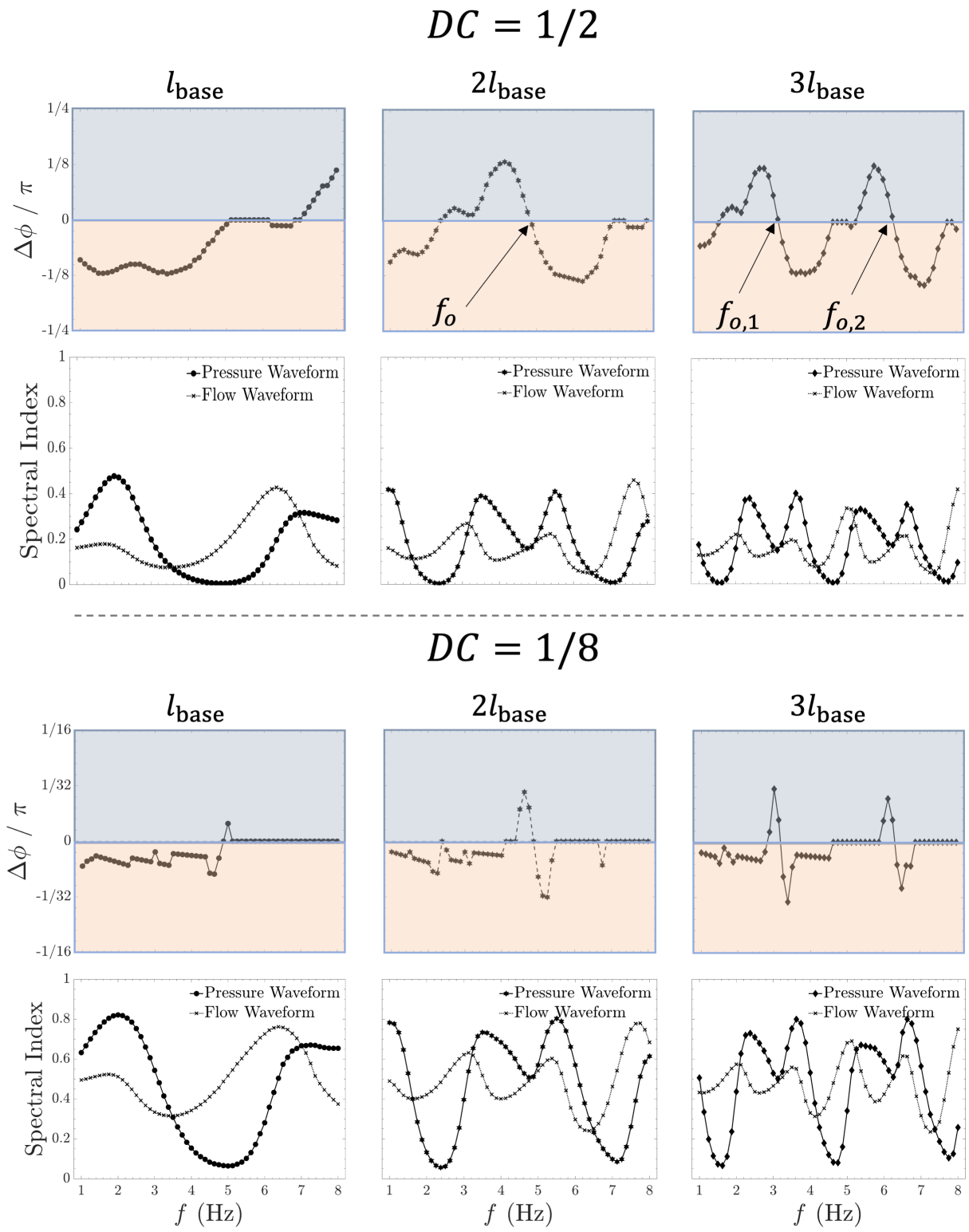

FIG. 8. Simulated phase delay and spectral index as a function of inflow frequency for two different duty cycles of values $DC = 1/2$ and $DC = 1/8$. The tube lengths and reflection coefficients correspond to same as those of figures 5-6.

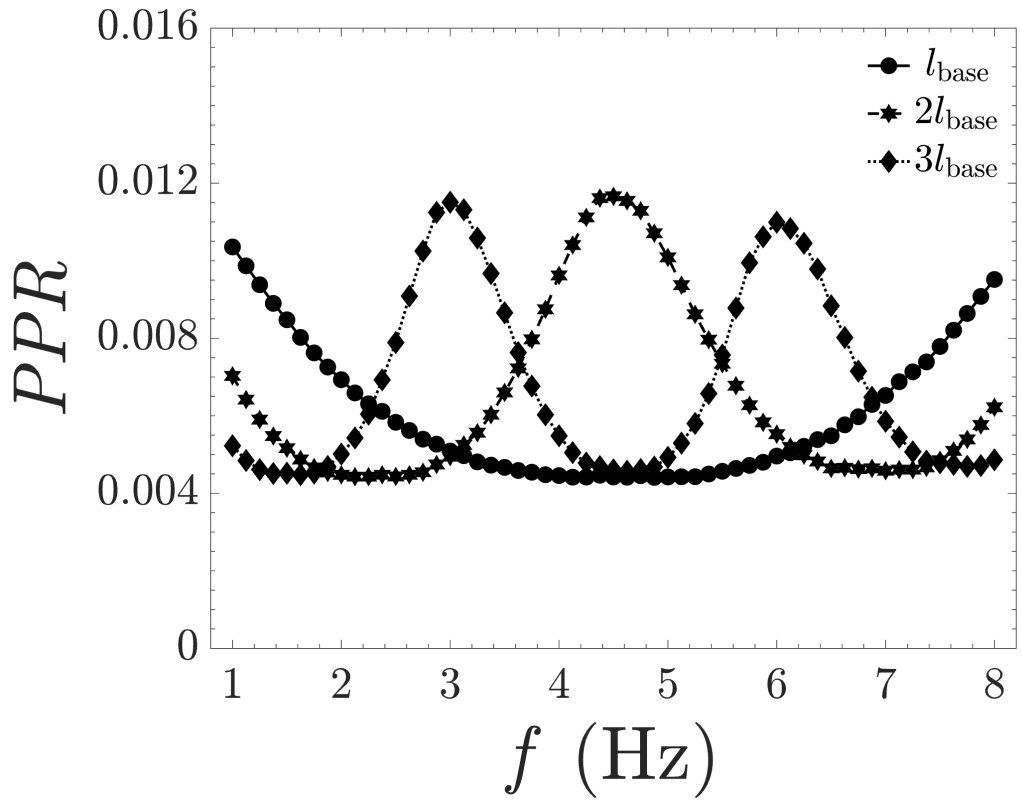

FIG. 9. The pulsatile power ratio (PPR) as a function of inflow frequency f for three tube lengths that are multiplicative factors of the baseline length l_{base} given in table I. For all simulations, the same inflow waveform of duty cycle $DC = 1$ and the same reflection coefficient of $\Gamma = 0.5$ have been employed.

C. Effect of reflection coefficient

Figure 10 presents the lowest value of the wave condition number [62] (i.e., the frequency at which the minimum PPR is found, scaled by the ratio of the tube length to the wave speed; $\widetilde{f_0} = f_0 \cdot L/c$), and its corresponding PPR value, as a function of reflection coefficient at the outlet of the primary tube (i.e., at the bifurcation interface). Such non-dimensionalization is inspired by previous works in literature [62, 63]. Different levels of reflection coefficients are achieved by fixing the primary tube stiffness at baseline and varying (increasing) the stiffnesses of the terminal boundary tubes. Results suggest an existence of different regimes of constant optimum frequency, with the higher reflection coefficients producing a significantly smaller frequency value even though the primary tube physical characteristics remain fixed. Note that the defined optimum frequency is within the range considered (see table I) to ensure physiological relevance. Results further suggest that increasing the reflection coefficient does not necessarily lead to an increase in the pulsatile load on the inlet (consistent with other studies [61]). Such findings imply that in the design of fluid-filled elastic tubes, the location of these optimum frequencies that minimize the pulsatile load on the flow generator (pump) can be controlled by varying the reflection coefficient. Such optimization requires identifying the frequency point of transition from the flow-leading to the pressure-leading regimes (see figure 6).

Figure 11 further investigates the effect, as a function of frequency, of the primary tube wave speed (columns) on PPR for different reflection coefficients (rows). At baseline wave speed, each power-frequency plots also include an inset plot of the phase delay between pressure and flow for reference. Results suggest that at a fixed reflection coefficient, an increase in the wave speed of the primary tube (achieved by increasing stiffness) can lead to an elevated pulsatile load on the input flow generator at all frequencies. On the other hand, at a fixed wave speed, changes in the reflection coefficient may not necessarily lead to an increase in the pulsatile load at some frequencies.

Figure 12 further explores the influence of the primary tube material properties by presenting the lowest value of the wave condition number as a function of wave speed for a fixed reflection coefficient of $\Gamma = 0.4$. The included inset plot provides the corresponding phase delay profiles for three representative wave speeds. Results illustrate a decrease in the corresponding wave condition number for increasing wave speed. However, this decrease is slight, implying that

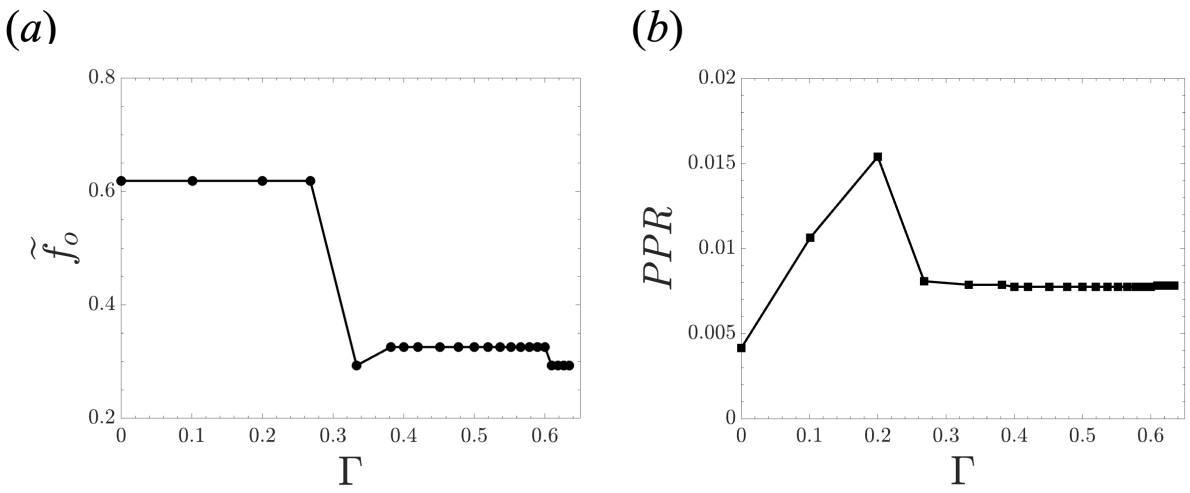

FIG. 10. (a) The lowest value of the wave condition number (i.e., the frequency at which the minimum pulsatile power is found, scaled by the ratio of the tube length to the wave speed: $\widetilde{f}_0 = f_0 \cdot L/c$) and (b) their corresponding pulsatile power ratios (PPRs) as a function of reflection coefficient at the primary tube outlet. For all simulations, the same inflow waveform of duty cycle $DC = 1$ has been employed.

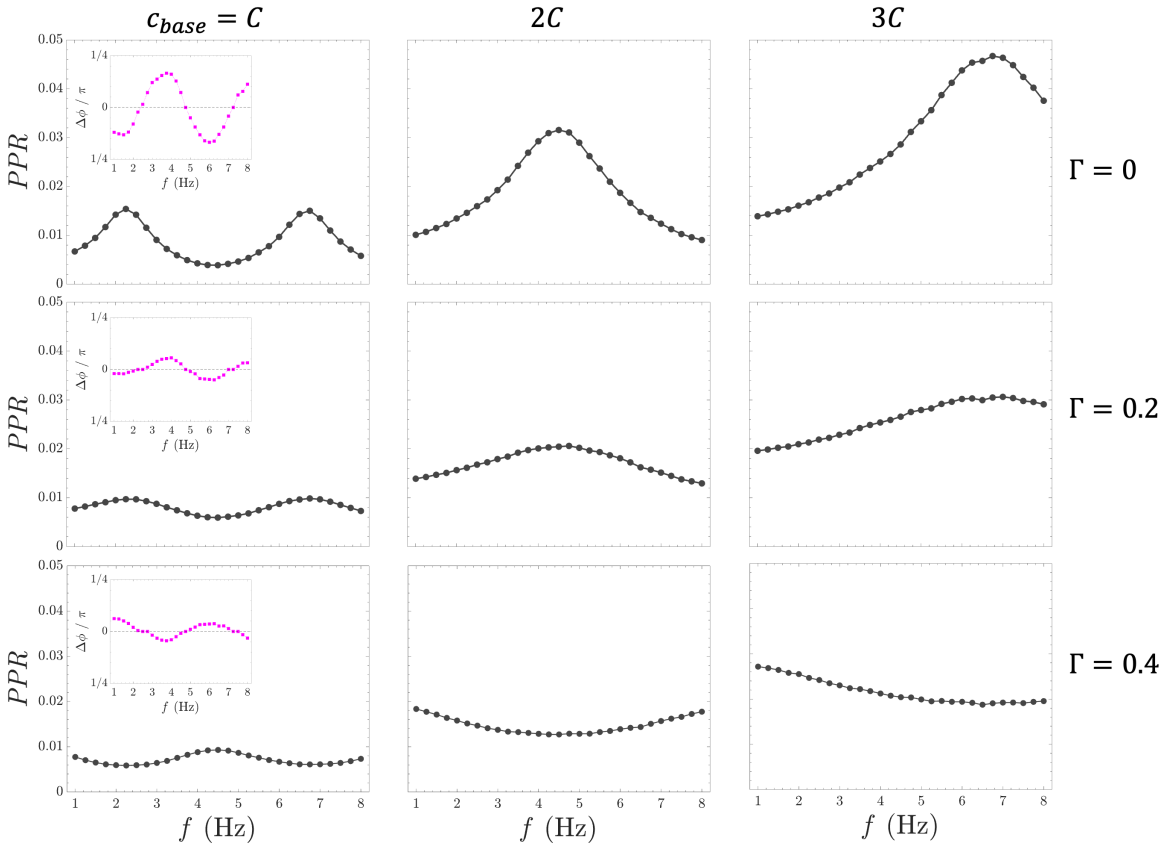

FIG. 11. Pulsatile power ratio (PPR) as a function of inflow frequency for different integer multiples of baseline primary tube wave speed (columns) and different reflection coefficients (rows). For all simulations, the same inflow waveform of duty cycle $DC = 1$ has been employed.

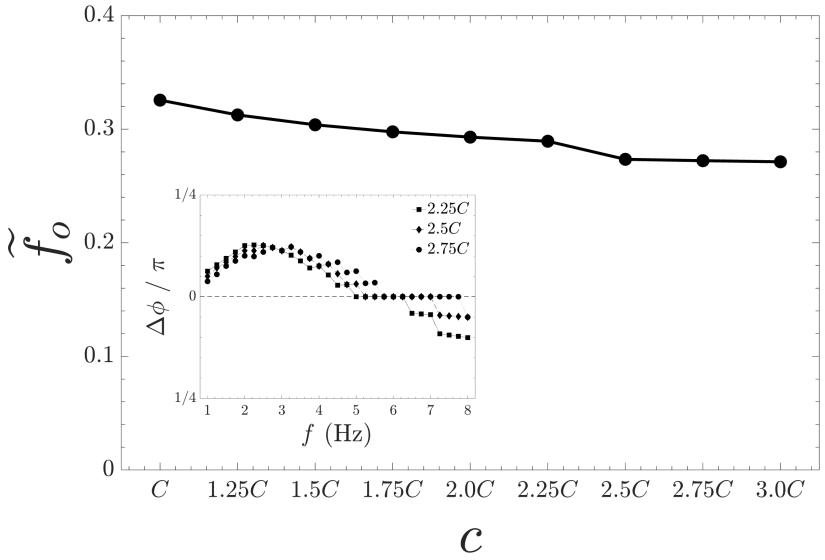

FIG. 12. The lowest value of the wave condition number (i.e., non-dimensionalised optimum inflow frequency parameter) as a function of the primary tube wave speed phase delay profiles of three representative cases (inset). For all simulations, the same inflow waveform of duty cycle $DC = 1$ and the same reflection coefficient of $\Gamma = 0.4$ have been employed.

the dependency of the optimum frequency on wave speed is not as significant as on the reflection coefficient (figure 10). This finding suggests that the reflection coefficient may offer a more favorable design criterion for controlling the optimum frequency in order to minimize possibly-destructive pulsatile loads on the inflow generator.

V. CONCLUSION

This work presents an analysis of wave reflection in fluid-filled compliant tubes and of its impact on pressure-flow wave propagation and input power expenditure. We have employed a recently-developed 1D (2D-axisymmetric) numerical model and have demonstrated that it effectively captures the same physical pressure-flow behavior as a 3D axisymmetric finite-element FSI solver, with both models showing similar frequency-dependent power characteristics. Through an extensive parameter exploration using the reduced-order approach, we have observed a nonlinear relationship between pulsatile power and inflow wave frequency that is influenced by parameters such as tube length and wave speed. Analysis of the phase delay between pressure and flow waves, along with their harmonic content, reveal two distinct regimes: a pressure-leading regime, where the pressure peak precedes the flow in time, and a flow-leading regime, where the flow peak leads that of the pressure. Our findings demonstrate that in the transition from a flow-leading regime to a pressure-leading regime (as a function of inflow frequency), there exist wave conditions at specific "optimum frequencies" at which the pulsatile load on the input (inflow generator) is minimized. Results further show that although such optimum frequencies are independent of the inflow wave profiles, they are highly dependent on reflection coefficients at the outlets. Understanding and identifying these optimum (inflow) frequencies may offer significant opportunities in pump engineering for minimizing pulsatile workload on flow generators. Moreover, our findings underscore the importance of the reflection coefficient as a determinant factor in design since it can enable control and adjustment of optimum frequencies. These insights are potentially useful in wave pumping considerations such as those related to the design of medical devices for biological systems involving fluid-filled compliant tubes and those related to the design of impedance pumps [64, 65].

Appendix A: Details of the Fourier-continuation approach and solver convergence

This section briefly provides some details of the particular discrete continuation algorithm—known as the FC(Gram) method—that is invoked by the solver used in this study. Considering discrete function values $\mathbf{A} = (A(x_0),\ ...,\ A(x_{N-1}))^T$ of $A(x) = A(x,\ t_n)$ on a spatial discretization of size N, FC(Gram) projects small numbers d_ℓ and d_r of the leftmost and rightmost points of A onto an orthogonal Gram polynomial basis. For example, at the left, such a basis can be constructed by orthonormalizing (e.g., via high-precision Gram-Schmidt) a Vandermonde

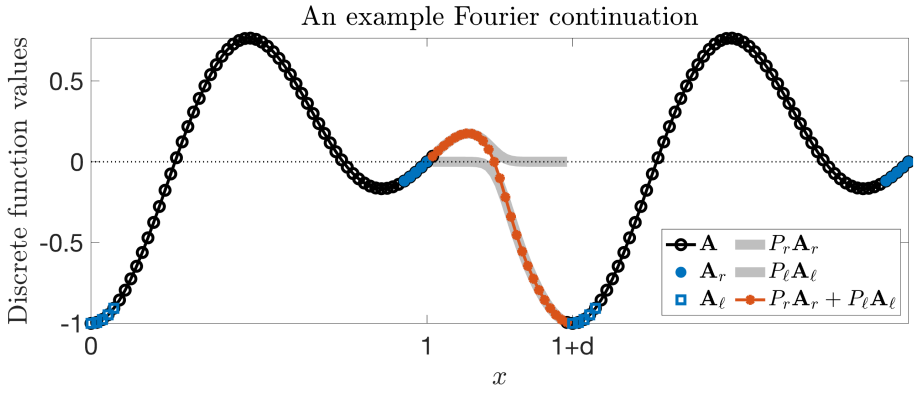

FIG. 13. An example illustration of the Fourier continuation method for a non-periodic function $A(x) = 1 - x^2 sin(2\pi x - \pi/2)$, $x \in [0, 1]$. The operators P_ℓ, P_r construct extensions that blend to zero via a basis of continuations that are precomputed. The resulting function is discretely periodic on the marginally larger interval given by $[0, 1 + \mathrm{d}]$.

matrix of point values at $x_0, ..., x_{d_\ell - 1}$ of the monomials $1,\ x,\ x^2,\ ...,\ x^{d_\ell - 1}$ (similarly for the right). This produces a projection operator Q_ℓ (respectively Q_r) onto the Gram basis. Each of the corresponding orthogonal Gram polynomials possesses a precomputed discrete continuation that blends its values to zero over an interval of length C points, and hence the projections provide the coefficients of this precomputed "continuation basis" that smoothly transition the leftmost d_ℓ values of $\mathbf{A}$ to zero (similarly for the rightmost d_r values). The sum of the leftward and rightward extensions constitutes the full Fourier continuation of discrete length $N + C$. Defining vectors of the d_ℓ leftmost and d_r rightmost function values by

$$\mathbf{A}_\ell \ = \ (A(x_0),\ A(x_1),\ ...,\ A(x_{d_\ell - 1}))^T \tag{A1}$$

and

$$\mathbf{A}_r \ = \ (A(x_{N-d_r}),\ A(x_{N-d_r+1}),\ ...,\ A(x_{N-1}))^T, \tag{A2}$$

the complete FC operation can be summarized by the expression

$$\widetilde{\mathbf{A}} \ = \ \begin{pmatrix} \mathbf{A} \\ B_\ell Q_\ell^T \mathbf{A}_\ell + B_r Q_r^T \mathbf{A}_r \end{pmatrix} = \begin{pmatrix} \mathbf{A} \\ P_\ell \mathbf{A}_\ell + P_r \mathbf{A}_r \end{pmatrix}, \tag{A3}$$

where B_ℓ, B_r contain the corresponding C values that blend (to zero) the left and the right Gram basis vectors. The final $\widetilde{\mathbf{A}}$ is a discrete vector of $N + C$ function values that matches $\mathbf{A}$ but that is periodic on a slightly larger interval (an additional C points). The coefficients of the series representations given by equation (7) can then be obtained by application of the FFT to $\widetilde{\mathbf{A}}$. Figure 13 provides an example Fourier continuation that illustrates the overall procedure outlined above. The particular solver employed in this work uses $d_\ell = d_r = 5$ matching points and $C = 25$ points to affect the continuation, resulting in fifth-order accuracy [44, 45, 54]. Full details on the specific algorithmic construction of the FC operators B_ℓ and B_r (and hence P_ℓ and P_r) have been given previously [44, 45, 54].

This section further considers the well-established method of manufactured solutions [66] (MMS) in order to assess numerical errors for verifying convergence and accuracy of the numerical solver employed in this study. Such a method postulates smooth solutions $A = A_{MMS}$ and $U = U_{MMS}$ of the governing PDE system of equation (1) with a non-homogeneous right-hand-side (RHS), i.e.,

$$\begin{pmatrix} \dfrac{\partial A}{\partial t}\,(x,\ t) \\ \dfrac{\partial U}{\partial t}\,(x,\ t) \end{pmatrix} + \begin{pmatrix} \dfrac{\partial\,(AU)}{\partial x}\,(x,\ t) \\ U\dfrac{\partial U}{\partial x}\,(x,\ t) + \dfrac{1}{\rho}\dfrac{\partial P}{\partial x}\,(x,\ t) + \dfrac{2\,(\xi+2)\,\pi\mu U\,(x,\ t)}{\rho A\,(x,\ t)} \end{pmatrix} = \begin{pmatrix} f_1(x,\ t) \\ f_2(x,\ t) \end{pmatrix}, \tag{A4}$$

which, upon substitution of $A = A_{MMS}$ and $U = U_{MMS}$, incorporates the remainder terms as a non-trivial forcing $(f_1(x,\ t),\ f_2(x,\ t))^T$. The resulting system enables the proposed functions, together with appropriate initial and

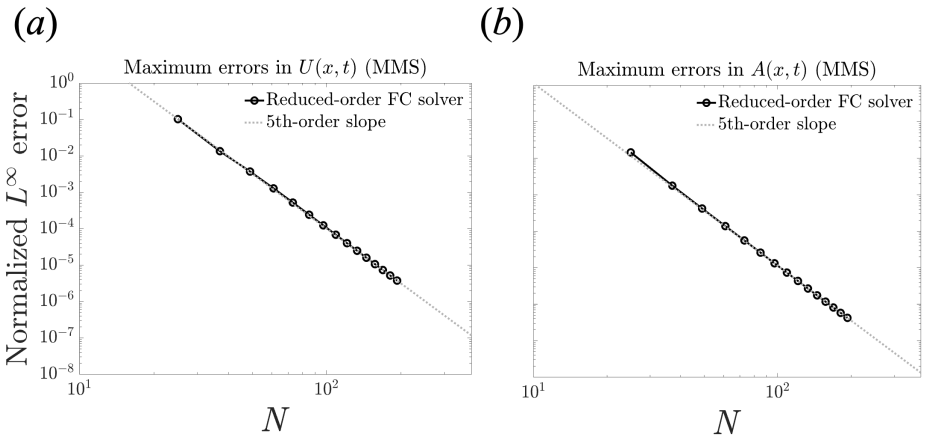

FIG. 14. Maximum errors (over all space and time) during one complete cycle ($t \in [0, 1]$) of velocity $U(x, t)$ (left) and area $A(x, t)$ (right) simulated by the FC solver applied to the manufactured right-hand-side corresponding to the exact solution. Timesteps are chosen small enough for each Δx so that errors are dominated by the spatial discretization (up to 64,000 timesteps). The overlaid dashed lines (slopes) demonstrate the high-order accuracy (i.e., fifth-order) of the numerical method employed in this work.

boundary conditions derived from them, to be exact solutions of a "forced" system given by equation (A4). In what follows, one considers the postulated solution to A and U on $x \in [0,\ 20\ \text{cm}]$ as

$$\begin{pmatrix} A\,(x,\ t) \\ U\,(x,\ t) \end{pmatrix} = \begin{pmatrix} A_{MMS}\,(x,\ t) \\ U_{MMS}\,(x,\ t) \end{pmatrix} = \quad \begin{pmatrix} a_1 \sin\left(k_1 x - \omega_1 t\right) \cos\left(k_2 x - \omega_2\,(t - t_1)\right) + a_2 \\ a_3 \sin\left(k_3 x + \omega_3 t\right) \cos\left(k_4 x + \omega_4\,(t - t_2)\right) + a_4 \end{pmatrix}, \tag{A5}$$

for parameters

$$\begin{pmatrix} a_1 \\ a_2 \\ a_3 \\ a_4 \end{pmatrix} = \begin{pmatrix} 1 \times 10^{-3} \\ 2 \times 10^{-3} \\ -0.5 \\ 0.1 \end{pmatrix}, \quad \begin{pmatrix} k_1 \\ k_2 \\ k_3 \\ k_4 \end{pmatrix} = \begin{pmatrix} 85\pi/6 \\ 25\pi/3 \\ 5\pi \\ 15\pi/2 \end{pmatrix}, \quad \begin{pmatrix} \omega_1 \\ \omega_2 \\ \omega_3 \\ \omega_4 \end{pmatrix} = \begin{pmatrix} 6\pi \\ 6\pi \\ 4\pi \\ 4\pi \end{pmatrix}, \quad \begin{pmatrix} t_1 \\ t_2 \end{pmatrix} = \begin{pmatrix} -\pi/5 \\ -\pi/7 \end{pmatrix}. \tag{A6}$$

Here, the area and velocity waves travel in different directions (rightward and leftward, respectively). Boundary conditions at $x = 0$ and $x = L = 20$ cm are hence given respectively by

$$\begin{pmatrix} A\,(0,\ t) \\ U\,(0,\ t) \end{pmatrix} = \begin{pmatrix} a_1 \sin\left(-\omega_1 t\right) \cos\left(-\omega_2\,(t - t_1)\right) + a_2 \\ a_3 \sin\left(\omega_3 t\right) \cos\left(\omega_4\,(t - t_2)\right) + a_4 \end{pmatrix}, \tag{A7}$$

$$\begin{pmatrix} A\,(L,\ t) \\ U\,(L,\ t) \end{pmatrix} = \begin{pmatrix} a_1 \sin\left(k_1 L - \omega_1 t\right) \cos\left(k_2 L - \omega_2\,(t - t_1)\right) + a_2 \\ a_3 \sin\left(k_3 L + \omega_3 t\right) \cos\left(k_4 L + \omega_4\,(t - t_2)\right) + a_4 \end{pmatrix}, \tag{A8}$$

and the corresponding initial conditions evaluated at $t = 0$ by

$$\begin{pmatrix} A\,(x,\ 0) \\ U\,(x,\ 0) \end{pmatrix} = \begin{pmatrix} a_1 \sin\left(k_1 x\right) \cos\left(k_2 x - \omega_2 t_1\right) + a_2 \\ a_3 \sin\left(k_3 x\right) \cos\left(k_4 x + \omega_4 t_2\right) + a_4 \end{pmatrix}. \tag{A9}$$

Applying the FC solver for one complete cycle ($0 \leq t \leq 1$) on a series of discretizations corresponding to integer multiples of $N = 12$ discretization points (where all timesteps are chosen small enough so that errors are dominated by spatial discretizations—for up to 64,000 timesteps), figure 14 presents the maximum absolute L^∞ errors (normalized to unity, i.e., a percentage) over all space and time for FC-based simulations of velocity $U(x,\ t)$ (left) and area $A(x, t)$ (right) approximating the exact MMS solutions given by equation (A5). The overlaid slopes demonstrate fifth-order accuracy of the solver as expected from the FC parameters employed in this study.

Appendix B: Additional validation test cases

Figure 15 compares the normalized pressure waveforms at the inlet of a fluid-filled compliant tube connected to a reflection site with a reflection coefficient of $\Gamma = 0.2$. The pressure profiles are generated using the reduced-order

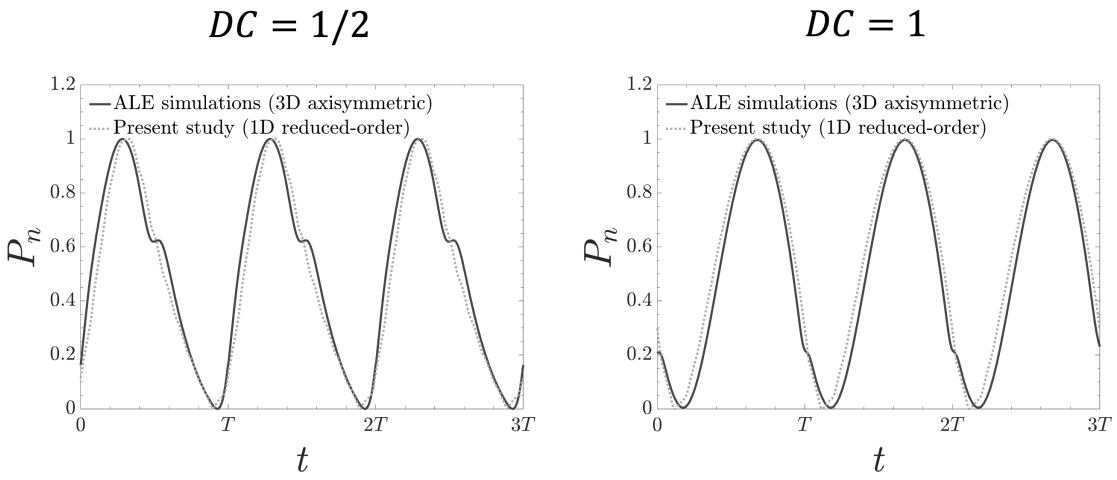

FIG. 15. Normalized pressure waveforms at the inlet for a fluid-filled compliant tube (connected to a reflection site with reflection coefficient $\Gamma = 0.2$) simulated by the solver employed in this paper (dotted line) and by a 3D FSI solver (solid line) at duty cycles (DC) of 1/2 and 1.

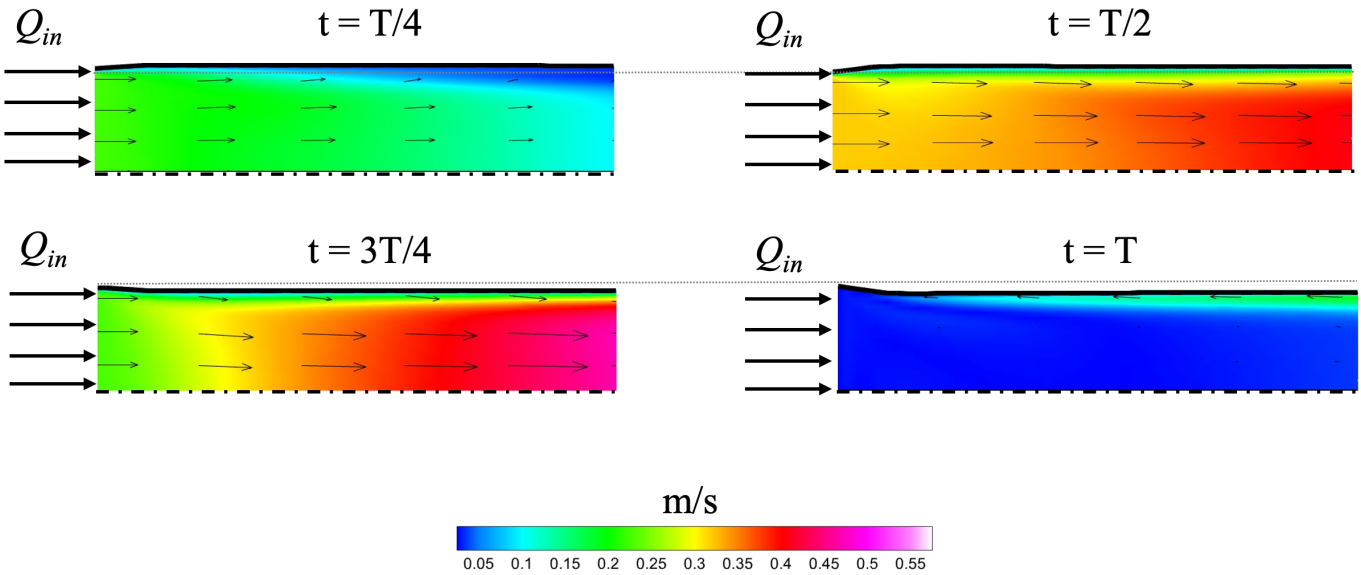

FIG. 16. Spatial distribution (pseudocolor plot) of fluid velocity amplitude simulated by the reference 3D axisymmetric ALE solver. Velocity vectors are overlaid as arrows. T represents the length of a full cycle and the dashed horizontal line represents the axis of symmetry. Results correspond to a flow source at a frequency of $f = 5$ Hz and $DC = 1$.

solver with bifurcations employed in this study (dotted line) and a 3D FSI solver (solid line) for two cases: a duty cycle of $DC = 1/2$ and a duty cycle of $DC = 1$. The figure highlights the strong agreement between the two solvers, demonstrating the validity of the reduced-order model for capturing the dynamics of more complex configurations involving wave reflections. Figure 16 presents fluid velocity amplitudes in the first quarter of the spatial domain at various snapshots in time (cycle length T) simulated by the reference 3D axisymmetric ALE solver for an inflow profile corresponding to $DC = 1$ and $f = 5$ Hz. The upper grey line in each figure corresponds to the initial wall position.

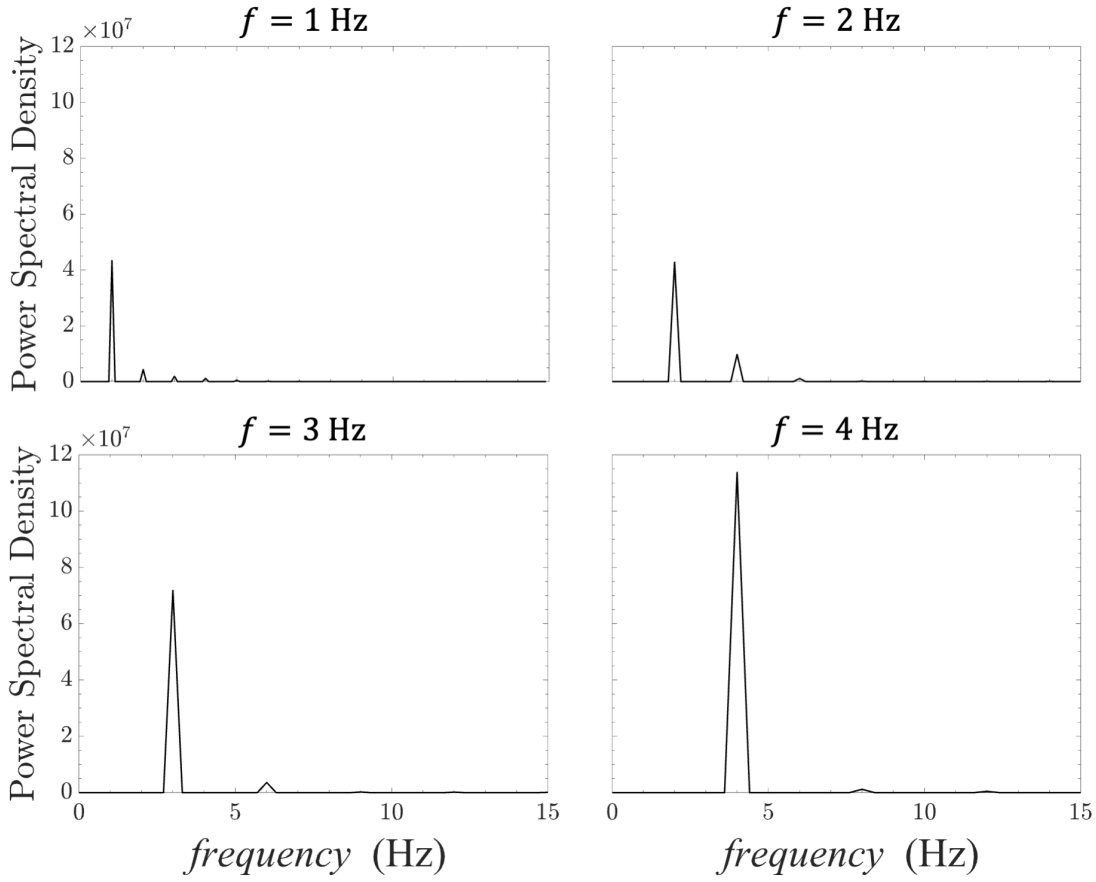

FIG. 17. The power spectral density (via FFT) of the pressure waveform at four sample inflow frequencies of $f = 1$ Hz, 2 Hz, 3 Hz, and 4 Hz. These curves corresponds to the pressure profiles presented in figure 4.

Appendix C: Sample cases of the power spectral density and phase curves

Figure 17 presents the frequency spectra of the oscillatory portion of the pressure profile obtained by FFTs at four sample inflow frequencies corresponding to figure 4. To evaluate the waveform morphology, the spectral index is defined based on this power spectral curve as the ratio of the power density of the second harmonic to that of the sum of the first and second harmonics. This definition relies on the two dominant harmonic modes since the contribution of higher harmonics to the power spectrum is not significant (as evidenced in figure 17). Figure 18 presents two illustrative examples of a positive phase delay ($\Delta\phi > 0$) and negative phase delay ($\Delta\phi < 0$) based on the pressure and flow waves relationship. Lastly, figure 19 presents the phase delay between pressure and flow at different tube lengths in the presence of the reflection coefficient of $\Gamma = 0.5$.

[1] F. N. Van de Vosse and N. Stergiopulos, Pulse wave propagation in the arterial tree, Annual Review of Fluid Mechanics **43**, 467 (2011).
[2] A. S. Forouhar, M. Liebling, A. Hickerson, A. Nasiraei-Moghaddam, H.-J. Tsai, J. R. Hove, S. E. Fraser, M. E. Dickinson, and M. Gharib, The embryonic vertebrate heart tube is a dynamic suction pump, Science **312**, 751 (2006).
[3] M. Zamir, On fractal properties of arterial trees, Journal of theoretical biology **197**, 517 (1999).
[4] A. Aghilinejad, F. Amlani, K. S. King, and N. M. Pahlevan, Dynamic effects of aortic arch stiffening on pulsatile energy transmission to cerebral vasculature as a determinant of brain-heart coupling, Scientific Reports **10**, 8784 (2020).
[5] D. M. Andrade, F. B. de Freitas Rachid, and A. S. Tijsseling, An analysis of fluid–structure interaction coupling mechanisms in liquid-filled viscoelastic pipes subject to fast transients, Journal of Fluids and Structures **121**, 103924 (2023).
[6] N. M. Pahlevan and M. Gharib, Aortic wave dynamics and its influence on left ventricular workload, PloS One **6**, e23106 (2011).

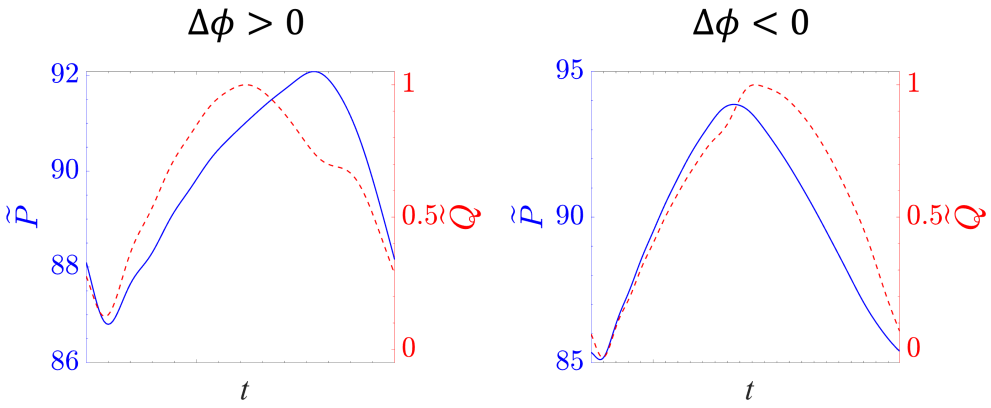

FIG. 18. Pressure (solid lines) and flow (dashed lines) waveforms at the measurement site (see figure 1) after reaching an oscillatory steady-state for two cases: a negative phase delay ($\Delta\phi < 0$) signifying that the pressure peak wave leads the flow wave in time (pressure-leading regime) and a positive phase delay ($\Delta\phi > 0$) indicating that the flow peak wave leads the pressure wave in time (flow-leading regime).

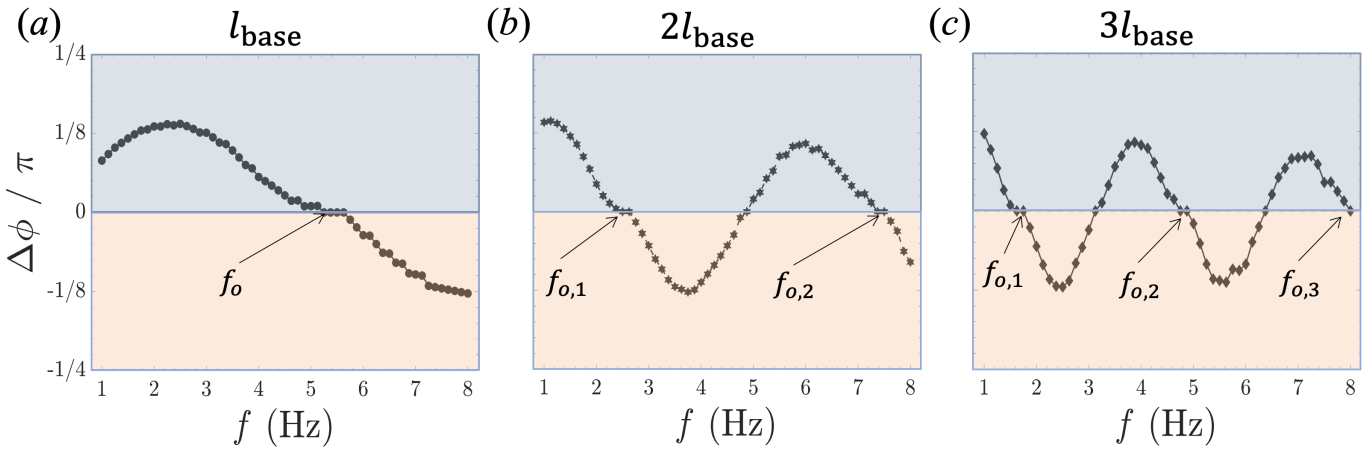

FIG. 19. The phase delay between pressure and flow at (a) baseline primary tube lengths, (b) twice the baseline primary tube length, and (c) three times the baseline primary tube length. For all simulations, the same inflow waveform of duty cycle $DC = 1$ and the same reflection coefficient of $\Gamma = 0.5$ have been employed.

[7] C. M. Quick, D. S. Berger, and A. Noordergraaf, Constructive and destructive addition of forward and reflected arterial pulse waves, American Journal of Physiology-Heart and Circulatory Physiology **280**, H1519 (2001).
[8] K. Menon, Z. Hu, and A. L. Marsden, Cardiovascular fluid dynamics: a journey through our circulation, Flow **4**, E7 (2024).
[9] M. F. O'Rourke, Steady and pulsatile energy losses in the systemic circulation under normal conditions and in simulated arterial disease, Cardiovascular research **1**, 313 (1967).
[10] N. Song, A. I. Adji, S. L. Hungerford, M. J. Namasivayam, C. S. Hayward, A. Jabbour, and D. W. Muller, Pulsatile energy consumption as a surrogate marker for vascular afterload improves with time post transcatheter aortic valve replacement in patients with aortic stenosis, Hypertension Research **46**, 730 (2023).
[11] R. Rasooli, O. Dur, and K. Pekkan, Estimation of pulsatile energy dissipation in intersecting pipe junctions using inflow pulsatility indices, AIP Advances **11** (2021).
[12] M. Zamir and R. Budwig, Physics of pulsatile flow, Appl. Mech. Rev. **55**, B35 (2002).
[13] J. P. Mynard, A. Kondiboyina, R. Kowalski, M. M. Cheung, and J. J. Smolich, Measurement, analysis and interpretation of pressure/flow waves in blood vessels, Frontiers in Physiology **11**, 1085 (2020).
[14] A. Aghilinejad, H. Wei, and N. M. Pahlevan, Non-invasive pressure-only aortic wave intensity evaluation using hybrid fourier decomposition-machine learning approach, IEEE Transactions on Biomedical Engineering **70**, 2139 (2023).
[15] A. Aghilinejad, F. Amlani, J. Liu, and N. M. Pahlevan, Accuracy and applicability of non-invasive evaluation of aortic wave intensity using only pressure waveforms in humans, Physiological Measurement **42**, 105003 (2021).
[16] A. Aghilinejad and M. Gharib, Assessing pressure wave components for aortic stiffness monitoring through spectral regression learning, European Heart Journal Open **4** (2024).

[17] D. M. Andrade, F. B. de Freitas Rachid, and A. S. Tijsseling, A new model for fluid transients in piping systems taking into account the fluid–structure interaction, Journal of Fluids and Structures **114**, 103720 (2022).

[18] T. Young, Xiii. hydraulic investigations, subservient to an intended croonian lecture on the motion of the blood, Philosophical Transactions of the Royal Society of London , 164 (1808).

[19] H. Resal, Note on the small motions of incompressible fluids in an elastic tube, Journal de Mathematiques Pures et Appliquees **3**, 342 (1876).

[20] A. I. Moens, *Die pulscurve* (Brill, 1878).

[21] v. D. Korteweg, Ueber die fortpflanzungsgeschwindigkeit des schalles in elastischen röhren, Annalen der Physik **241**, 525 (1878).

[22] J. R. Womersley, Method for the calculation of velocity, rate of flow and viscous drag in arteries when the pressure gradient is known, The Journal of Physiology **127**, 553 (1955).

[23] S. I. Rubinow and J. B. Keller, Wave propagation in a viscoelastic tube containing a viscous fluid, Journal of Fluid Mechanics **88**, 181 (1978).

[24] E. Brocher, C. Maresca, and M.-H. Bournay, Fluid dynamics of the resonance tube, Journal of Fluid Mechanics **43**, 369 (1970).

[25] G. Herrmann and I. Mirsky, Three-Dimensional and Shell-Theory Analysis of Axially Symmetric Motions of Cylinders, Journal of Applied Mechanics **23**, 563 (1956).

[26] G. Kuiken, Wave propagation in a thin-walled liquid-filled initially stressed tube, Journal of Fluid Mechanics **141**, 289 (1984).

[27] R. Skalak, An extension of the theory of water hammer, Transactions of the American Society of Mechanical Engineers **78**, 105 (1956).

[28] L. Zhang, S. Tijsseling, and E. Vardy, FSI analysis of liquid-filled pipes, Journal of Sound and Vibration **224**, 69 (1999).

[29] A. Aghilinejad, R. Alavi, B. Rogers, F. Amlani, and N. M. Pahlevan, Effects of vessel wall mechanics on non-invasive evaluation of cardiovascular intrinsic frequencies, Journal of Biomechanics **129**, 110852 (2021).

[30] A. Aghilinejad, H. Wei, C. Bilgi, A. Paredes, A. DiBartolomeo, G. A. Magee, and N. M. Pahlevan, Framework development for patient-specific compliant aortic dissection phantom model fabrication: magnetic resonance imaging validation and deep-learning segmentation, Journal of Biomechanical Engineering **145**, 091010 (2023).

[31] A. Aghilinejad, C. Bilgi, H. Geng, and N. M. Pahlevan, Aortic stretch and recoil create wave-pumping effect: the second heart in the systemic circulation, Journal of The Royal Society Interface **22**, 20240887 (2025).

[32] I. Avrahami and M. Gharib, Computational studies of resonance wave pumping in compliant tubes, Journal of Fluid Mechanics **608**, 139 (2008).

[33] A. I. Hickerson and M. Gharib, On the resonance of a pliant tube as a mechanism for valveless pumping, Journal of Fluid Mechanics **555**, 141 (2006).

[34] E. Jung and C. S. Peskin, Two-dimensional simulations of valveless pumping using the immersed boundary method, SIAM Journal on Scientific Computing **23**, 19 (2001).

[35] C. G. Manopoulos, D. S. Mathioulakis, and S. G. Tsangaris, One-dimensional model of valveless pumping in a closed loop and a numerical solution, Physics of Fluids **18** (2006).

[36] A. Aghilinejad, B. Rogers, H. Geng, and N. M. Pahlevan, On the longitudinal wave pumping in fluid-filled compliant tubes, Physics of Fluids **35** (2023).

[37] R. A. Carmigniani, M. Benoit, D. Violeau, and M. Gharib, Resonance wave pumping with surface waves, Journal of Fluid Mechanics **811**, 1 (2017).

[38] N. Sarvazyan, Building valveless impedance pumps from biological components: Progress and challenges, Frontiers in Physiology **12**, 2407 (2022).

[39] A. I. Hickerson, D. Rinderknecht, and M. Gharib, Experimental study of the behavior of a valveless impedance pump, Experiments in Fluids **38**, 534 (2005).

[40] N. M. Pahlevan and M. Gharib, In-vitro investigation of a potential wave pumping effect in human aorta, Journal of Biomechanics **46**, 2122 (2013).

[41] A. Aghilinejad, F. Amlani, S. P. Mazandarani, K. S. King, and N. M. Pahlevan, Mechanistic insights on age-related changes in heart-aorta-brain hemodynamic coupling using a pulse wave model of the entire circulatory system, American Journal of Physiology-Heart and Circulatory Physiology **325**, H1193 (2023).

[42] J. Alastruey, A. W. Khir, K. S. Matthys, P. Segers, S. J. Sherwin, P. R. Verdonck, K. H. Parker, and J. Peiró, Pulse wave propagation in a model human arterial network: assessment of 1-D visco-elastic simulations against in vitro measurements, Journal of Biomechanics **44**, 2250 (2011).

[43] E. Boileau, P. Nithiarasu, P. J. Blanco, L. O. Müller, F. E. Fossan, L. R. Hellevik, W. P. Donders, W. Huberts, M. Willemet, and J. Alastruey, A benchmark study of numerical schemes for one-dimensional arterial blood flow modelling, International Journal for Numerical Methods in Biomedical Engineering **31**, e02732 (2015).

[44] F. Amlani and O. P. Bruno, An FC-based spectral solver for elastodynamic problems in general three-dimensional domains, Journal of Computational Physics **307**, 333 (2016).

[45] F. Amlani and N. M. Pahlevan, A stable high-order FC-based methodology for hemodynamic wave propagation, Journal of Computational Physics **405**, 109130 (2020).

[46] S. Z. Pagoulatou, M. Ferraro, B. Trachet, V. Bikia, G. Rovas, L. A. Crowe, J.-P. Vallee, D. Adamopoulos, and N. Stergiopulos, The effect of the elongation of the proximal aorta on the estimation of the aortic wall distensibility, Biomechanics and modeling in mechanobiology **20**, 107 (2021).

[47] A. Arzani and S. C. Shadden, Characterization of the transport topology in patient-specific abdominal aortic aneurysm models, Physics of Fluids **24** (2012).

[48] N. M. Pahlevan, F. Amlani, M. Hossein Gorji, F. Hussain, and M. Gharib, A physiologically relevant, simple outflow boundary model for truncated vasculature, Annals of biomedical engineering **39**, 1470 (2011).

[49] K. S. Matthys, J. Alastruey, J. Peiró, A. W. Khir, P. Segers, P. R. Verdonck, K. H. Parker, and S. J. Sherwin, Pulse wave propagation in a model human arterial network: assessment of 1-d numerical simulations against in vitro measurements, Journal of biomechanics **40**, 3476 (2007).

[50] J. P. Mynard and J. J. Smolich, One-dimensional haemodynamic modeling and wave dynamics in the entire adult circulation, Annals of Biomedical Engineering **43**, 1443 (2015).

[51] A. Aghilinejad, H. Wei, G. A. Magee, and N. M. Pahlevan, Model-based fluid-structure interaction approach for evaluation of thoracic endovascular aortic repair endograft length in type b aortic dissection, Frontiers in Bioengineering and Biotechnology **10**, 825015 (2022).

[52] B. Kim, W.-X. Huang, S. J. Shin, and H. J. Sung, Flexible ring flapping in a uniform flow, Journal of Fluid Mechanics **707**, 129 (2012).

[53] G. Michelson, J. Harazny, R. E. Schmieder, R. Berendes, T. Fiermann, and S. Wärntges, Fourier analysis of the envelope of the ophthalmic artery blood flow velocity: Age-and blood pressure–related impact, Hypertension **50**, 964 (2007).

[54] F. Amlani, H. Wei, and N. M. Pahlevan, A Fourier-based methodology without numerical diffusion for conducting dye simulations and particle residence time calculations, Journal of Computational Physics **493**, 112472 (2023).

[55] J. Kang, A. Aghilinejad, and N. M. Pahlevan, On the accuracy of displacement-based wave intensity analysis: Effect of vessel wall viscoelasticity and nonlinearity, PloS One **14**, e0224390 (2019).

[56] A. M. Bavo, G. Rocatello, F. Iannaccone, J. Degroote, J. Vierendeels, and P. Segers, Fluid-structure interaction simulation of prosthetic aortic valves: comparison between immersed boundary and arbitrary lagrangian-eulerian techniques for the mesh representation, PloS one **11**, e0154517 (2016).

[57] K.-J. Bathe, H. Zhang, and S. Ji, Finite element analysis of fluid flows fully coupled with structural interactions, Computers & Structures **72**, 1 (1999).

[58] N. Xiao, J. Alastruey, and C. Alberto Figueroa, A systematic comparison between 1-d and 3-d hemodynamics in compliant arterial models, International journal for numerical methods in biomedical engineering **30**, 204 (2014).

[59] Y.-c. Fung, *Biomechanics: circulation* (Springer Science & Business Media, 2013).

[60] M. Roknujjaman, H. Kyotoh, A. Yohei, and A. Yasuhisa, Experimental and theoretical analysis of pulsatile flow in elastic tubes: Wave propagation and attenuation, Physics of Fluids **35** (2023).

[61] N. M. Pahlevan and M. Gharib, A bio-inspired approach for the reduction of left ventricular workload, PloS One **9**, e87122 (2014).

[62] N. M. Pahlevan and M. Gharib, A wave dynamics criterion for optimization of mammalian cardiovascular system, Journal of Biomechanics **47**, 1727 (2014).

[63] B. Yigit and K. Pekkan, Non-dimensional physics of pulsatile cardiovascular networks and energy efficiency, Journal of The Royal Society Interface **13**, 20151019 (2016).

[64] M. F. O'Rourke, Towards optimization of wave reflection: therapeutic goal for tomorrow?, Clinical and Experimental Pharmacology & Physiology **23**, S11 (1996).

[65] A. D. Hughes, K. H. Parker, and J. E. Davies, Waves in arteries: a review of wave intensity analysis in the systemic and coronary circulations, Artery Research **2**, 51 (2008).

[66] P. J. Roache, Code verification by the method of manufactured solutions, Journal of Fluids Engineering **124**, 4 (2002).